

Response

We thank the Editor Dr. Tim Dunkerton for his thorough and constructive comments, which are very helpful in our further revision of the manuscript. We have made every effort to address all the concerns raised. Our point-by-point response is given below.

Addendum prior to final acceptance in ACP:

Some improvements and clarifications have been made in the revised version, in response to comments of reviewers, e.g., concerning methodology, phase relationships, and power spectra.

Although the paper is acceptable in its present form, my opinion is that the Abstract and opening paragraphs of the Conclusion merit some modification in order to reflect the significance of the main findings of the paper more fully and accurately. Therefore I am providing the authors with a final opportunity to improve the presentation of major findings in these two places of the manuscript.

It is important to take advantage of this opportunity because the field campaign is a significant investment of research dollars, and for this campaign in particular, gravity waves provide a focal point for study as part of the broader objective regarding Ex-UTLS transport processes.

Reply: We have followed the recommendations from the editor, and made corresponding changes in the abstract and conclusion to highlight the major achievements from the field experiment.

Here is an outline of my concerns and how the summary of findings can be modified:

1. The existing summary is quick to highlight measurement issues, and projects an overly negative tone. More emphasis is needed on positive findings.

Reply: Modified accordingly. Please check the revision in abstract and conclusion.

2. Among these positive findings is evidence of 50-500 km mesoscale fluctuations with the expected signature of vertically propagating gravity waves.

Reply: Modified accordingly. Please check the revision in abstract and conclusion.

3. Not all such fluctuations are consistent with a monochromatic wave, but admit other interpretations. For example, quadrature of u' and w' may indicate rolling turbulent motions in the vertical plane, such as inertial instability, or simply a superposition of upward and downward waves owing to reflection.

Reply: Modified accordingly. Please check the revision in abstract and conclusion.

4. Perhaps it is my misunderstanding, but the paper seems to confuse measurement issues with

45 *alternative (possibly true) explanations of deviations from gravity-wave behavior. By all means,*
46 *take care to disentangle the measurement issues from these alternative explanations.*

47
48 **Reply: It is indeed to our disappointment that these two issues are hard to separate based**
49 **on limited 1-D flight-track observations we made. We simply stated the two possibilities**
50 **though some wording is changed to avoid confusion. Please check the revision in abstract**
51 **and conclusion.**

52
53 *5. From prior conversation with the lead author several years ago, I understand his concern about*
54 *false signals owing to vertical fluctuations of aircraft motion. Unless I missed it, the paper*
55 *doesn't make completely clear whether the pressure measurements alone are vulnerable in this*
56 *respect, or if the problem spills over to the velocity component measurements. If necessary,*
57 *please clarify.*

58
59 **Reply: Yes, we still have strong concern on the measurement signals with sampled periods**
60 **of ~20~60 seconds and wavelengths of ~5~15 km. In particular, we have strong concern**
61 **on using the corrected static pressure P_c at the above-mentioned scale to understand**
62 **gravity waves, and the problem may spill over the velocity component, especially since**
63 **static pressure P_s and vertical motion w behave rather similarly to each other at the above-**
64 **mentioned scales (in other words, there is no strict constant P_s height assumption for the**
65 **disturbances at the above-mentioned scale). However, as seen in our response to your**
66 **previous comment, unfortunately we are not able to pinpoint whether these are**
67 **measurement errors or not.**

68
69 *6. Regarding power spectra, the revision has attempted to highlight the -3 power law in addition*
70 *to the -5/3 power law. A general summary of power spectra is as follows: (i) horizontal velocity*
71 *components at the larger mesoscales display the approximate -5/3 power law in agreement with*
72 *GASP & MOZAIC; (ii) vertical velocity is flat in this range; (iii) approaching smaller*
73 *mesoscales the fluctuations roll over to a -3 power law, except (iv) when this part of the*
74 *spectrum is activated, as recorded beautifully during M2. The following clip is noteworthy:*

75
76 *"Despite the overall resemblance among the flight segments of RF02, there are some unique*
77 *characteristics in the power spectral distributions for individual segments. For segments M1 and*
78 *M2, for example, (i.e., the fourth column versus the fifth column in Fig. 4), the slopes of u and v*
79 *during segment M1 are approximately consistent with a -3 power law for the scale of ~0.5~8*
80 *km, while those during segment M2 follows a -5/3 power law instead. This is probably*
81 *associated with the fact that segment M2 successfully captures a rapid decrease in u (from ~65*
82 *m/s to ~40 m/s) while segment M1 has no such a dramatic reduction in u (the fourth column in*
83 *Fig. 3a versus the fifth column in Fig. 3a). Note that the aircraft during segment M1 flew away*
84 *from the jet core region, as the jet was still moving eastward to the downhill side of the*
85 *topography. In contrast, the aircraft during segment M2 flew directly toward the approaching jet*
86 *core at a lower flight level than segment M1 (the fourth column in Fig. 3d versus the fifth column*
87 *in Fig. 3d), and the observed decline of u (i.e., a potential jet exit region) is located roughly on*
88 *the downhill side of the topography (the fifth column in Fig. 3d). This suggests that the spectral*
89 *slopes for the aircraft measurements can, in fact, be extremely sensitive to changes in the*
90 *background flow, even though sampling takes place in the same area only a few hours apart."*

91
92 *This example of activated spectrum is lost when the average is taken over all flight segments.*
93 *Interestingly, the M1 segment immediately prior to M2 did not record the event. By the way, it*
94 *should be noted (and stated explicitly, if not already) that the wavelet analysis doesn't reach into*
95 *this spectral range of elevated power. Either the orographic wave in question did not penetrate*
96 *to the flight level of M1, or it was excited suddenly as the jet approached from the west. By any*
97 *chance, however slight, could the model simulation resolve this ambiguity?*

98
99 **Reply: (1) Please check the revision in abstract and conclusion for the summary of power**
100 **spectra. (2) The reason why the elevated power is not clear in the wavelet analysis is that**
101 **the power for the scale below ~4km is not shown in the wavelet analysis, and the global**
102 **wavelet power is not calculated. Please note that the elevated power in the spectrum of M2**
103 **mainly occurs at the scale below ~4-8 km. (3) Unfortunately, our current simulation does**
104 **not have enough resolution to resolve this spectral range.**

105
106 *7. Regarding the -5/3 slope at larger mesoscales, clearly it cannot be attributed to isotropic 3D*
107 *turbulence. On the other hand, the activated spectrum at smaller mesoscales during might fit this*
108 *interpretation.*

109
110 **Reply: Agree. However, our recent separate study of the idealized moist baroclinic wave**
111 **spectra suggest that presence of moist convection and mesoscale gravity waves, though**
112 **non-isotropic, does appear to steer the mesoscale range of the spectral slope to be -5/3, even**
113 **though these waves are clearly not isotropic. Please check the revision in the conclusion.**

114
115 *In summary, I encourage the authors to address these concerns, mostly by way of additional*
116 *summary inserted in the Abstract and Conclusions. A final thought is:*

117
118 *8. Since we anticipate several follow-on studies of these unique measurements, a brief list at the*
119 *end of the Conclusion might highlight a few key issues and how they might be addressed.*

120
121 **Reply: We have added some future research directions and possibilities in the concluding**
122 **discussion.**

1 **Aircraft Measurements of Gravity Waves in the Upper Troposphere and Lower**
2 **Stratosphere during the START08 Field Experiment**

3
4 Fuqing Zhang^{1*}, Junhong Wei¹, Meng Zhang¹, Kenneth P. Bowman², Laura L. Pan³, Elliot
5 Atlas⁴, and Steve C. Wofsy⁵

- 6
7 1. Department of Meteorology, The Pennsylvania State University, University Park,
8 Pennsylvania
9 2. Department of Atmospheric Sciences, Texas A&M University, College Station, Texas
10 3. National Center for Atmospheric Research, Boulder, Colorado
11 4. Rosenstiel School of Marine and Atmospheric Science, University of Miami, Miami,
12 Florida
13 5. Division of Engineering and Applied Science/Department of Earth and Planetary
14 Science, Harvard University, Cambridge, Massachusetts

15
16
17 **Submitted to *Atmospheric Chemistry and Physics* for publication**

18 **Initial Submission, 3 November 2014**

19 **Revised submission, 28 December 2014**

20 **Final revision, 27 May 2015**

21
22
Junhong Wei 5/27/2015 8:57 AM

Deleted: 4

Corresponding author address: Professor Fuqing Zhang, Dept. of Meteorology, The Pennsylvania State University, University Park, PA 16802. E-mail: fzhang@psu.edu

24
25
26
27
28
29
30
31
32
33
34
35
36
37
38
39
40
41
42
43
44
45
46
47

Abstract

This study analyzes *in-situ* airborne measurements from the 2008 Stratosphere-Troposphere Analyses of Regional Transport (START08) experiment to characterize gravity waves in the extratropical upper troposphere and lower stratosphere (ExUTLS). The focus is on the second research flight (RF02), which took place on 21-22 April 2008. This was the first airborne mission dedicated to probing gravity waves associated with strong upper-tropospheric jet-front systems. Based on spectral and wavelet analyses of the *in-situ* observations, along with a diagnosis of the polarization relationships, clear signals of mesoscale variations with wavelengths ~50-500 km are found in almost every segment of the 8-hr flight, which took place mostly in the lower stratosphere. The aircraft sampled a wide range of background conditions including the region near the jet core, the jet exit and over the Rocky Mountains with clear evidence of vertically propagating gravity waves of along-track wavelength between 100 and 120 km. The power spectra of the horizontal velocity components and potential temperature for the scale approximately between ~8 km and ~256 km display an approximate -5/3 power law in agreement with past studies on aircraft measurements, while the fluctuations roll over to a -3 power law for the scale approximately between ~0.5 km and ~8 km (except when this part of the spectrum is activated, as recorded clearly by one of the flight segments). However, at least part of the high-frequency signals with sampled periods of ~20~60 seconds and wavelengths of ~5~15 km might be due to intrinsic observational errors in the aircraft measurements, even though the possibilities that these fluctuations may be due to other physical phenomena (e.g., nonlinear dynamics, shear instability and/or turbulence) cannot be completely ruled out.

Fuqing Zhang 5/24/2015 10:45 AM
Deleted: region

Junhong Wei 5/27/2015 9:11 AM
Deleted:

Fuqing Zhang 5/24/2015 10:50 AM
Deleted: Regarding

Fuqing Zhang 5/24/2015 10:50 AM
Deleted: ,

Fuqing Zhang 5/24/2015 10:50 AM
Deleted: the

Fuqing Zhang 5/24/2015 10:51 AM
Deleted: and

Fuqing Zhang 5/24/2015 10:46 AM
Deleted: beautifully

Fuqing Zhang 5/24/2015 10:50 AM
Deleted: In addition, among the positive findings is evidence of vertically propagating gravity waves of along-track wavelength between 100 and 120 km, as well as evidence of vertically trapped gravity waves of along-track wavelength between 32 and 64 km. In contrast to the long wavelength mesoscale variations, smaller-scale wavelike oscillations below 50 km are found to be quite transient.

Junhong Wei 5/23/2015 11:45 AM
Deleted: In particular

Fuqing Zhang 5/24/2015 11:04 AM
Deleted: aircraft measurements of several flight segments are dominated by signals

Fuqing Zhang 5/24/2015 10:54 AM
Deleted: (assuming that the typical flight speed is approximately 250 m/s). We speculate that at least part of these nearly-periodic high-frequency signals are

Fuqing Zhang 5/24/2015 11:03 AM
Deleted: a result of

Fuqing Zhang 5/24/2015 11:04 AM
Deleted: or small-scale flight-altitude fluctuations that are difficult to fully characterize

Junhong Wei 5/23/2015 4:46 PM
Deleted: .

Fuqing Zhang 5/24/2015 11:05 AM
Deleted: o

Junhong Wei 5/23/2015 10:35 AM
Deleted: Despite the presence of possibly spurious wave oscillations in several flight segments, the power spectra of horizontal winds and temperature averaged over the analyzed START08 flight segments generally follow the -5/3 power law.

83 **1. Introduction**

84 One of the challenges to understanding the extratropical upper troposphere and lower
85 stratosphere (ExUTLS) is that dynamical processes with a wide range of scales occur in the
86 region. Gravity waves, in particular, are known to play a significant role in determining the
87 structure and composition of the ExUTLS. Tropopause jets and fronts are significant sources of
88 gravity waves (O’Sullivan and Dunkerton 1995; Reeder and Griffins 1996; Zhang 2004; Wang
89 and Zhang 2007; Mirzaei et al. 2014; Wei and Zhang 2014, 2015), along with surface
90 topography (Smith 1980) and moist convection (Lane et al. 2001). Gravity waves above the jet
91 may be responsible for double or multiple tropopauses (Yamanaka et al. 1996; Pavelin et al.
92 2001) and may contribute to layered ozone or PV structures (Bertin et al. 2001). Also, strong
93 horizontal and vertical shear in the layer and the discontinuity in static stability at the tropopause
94 provide a favorable environment to reflect, capture, break and dissipate gravity waves generated
95 in the lower troposphere, such as those produced by surface fronts (Plougonven and Snyder
96 2007). Gravity wave breaking and wave-induced turbulence (e.g., Koch et al. 2005) can
97 contribute significantly to mixing of trace gases in the ExUTLS, thereby affecting chemical
98 composition (Vaughan and Worthington, 2000). Also, convectively-generated gravity waves
99 may extend the impact of moist convection far above cloud tops through wave-induced mixing
100 and transport (Lane et al. 2004).

101 In particular, mesoscale gravity waves with horizontal wavelength of ~50~500 km are
102 known to occur in the vicinity of unbalanced upper-tropospheric jet streaks and on the cold-air
103 side of surface frontal boundaries (Uccellini and Koch 1987; Plougonven and Zhang 2014). This
104 phenomenon has been identified repeatedly in both observational studies (Uccellini and Koch
105 1987; Schneider 1990; Fritts and Nastrom 1992; Ramamurthy et al. 1993; Bosart et al. 1998;

106 Koppel et al. 2000; Rauber et al. 2001; Plougonven et al. 2003) and numerical investigations of
107 the observed cases (Powers and Reed 1993; Pokrandt et al. 1996; Kaplan et al. 1997; Zhang and
108 Koch 2000; Zhang et al. 2001, 2003; Koch et al. 2001, 2005; Lane et al. 2004). In addition,
109 idealized simulations of dry baroclinic jet-front systems in a high-resolution mesoscale model
110 have been performed to investigate the generation of mesoscale gravity waves (Zhang 2004), the
111 sensitivity of mesoscale gravity waves to the baroclinicity of jet-front systems (Wang and Zhang
112 2007), and the source of gravity waves with multiple horizontal scales (Lin and Zhang 2008).
113 Most recently, Wei and Zhang (2014, 2015) studied the characteristics and potential source
114 mechanisms of mesoscale gravity waves in moist baroclinic jet-front systems with varying
115 degree of convective instability.

116 Advances in space technology provide the means to observe gravity waves in detail.
117 Recent studies have demonstrated that satellites such as Microwave Limb Sounder (MLS) and
118 Advanced Microwave Sounding Unit-A (AMSU-A) offer quantitative information of gravity
119 waves in the middle atmosphere (Alexander and Rosenlof 2003; Wu and Zhang 2004; Zhang et
120 al. 2013). In addition to satellite measurements, gravity waves are also observed by surface
121 observations (Einaudi et al. 1989; Grivet-Talocia et al. 1999; Koppel et al. 2000), high-resolution
122 radionsonde networks (Vincent and Alexander 2000; Wang and Geller 2003; Zhang and Yi
123 2007; Gong and Geller 2010), radars (Vaughan and Worthington 2000, 2007), and super-
124 pressure balloons (Hertzog and Vial 2001).

125 Among the abovementioned observational tools, aircraft have also been widely used as
126 *in-situ* measurements of gravity waves. Probably since Radok (1954), which was one of the first
127 observations of mountain waves with aircraft, past aircraft field campaigns have mainly focused
128 on terrain-induced gravity waves (Radok 1954; Vergeiner and Lilly 1970; Lilly and Kennedy

129 1973; Smith 1976; Karacostas and Marwitz 1980; Brown 1983; Moustouei et al. 1999;
130 Leutbecher and Volkert 2000; Poulos et al. 2002; Dornbrack et al. 2002; Doyle et al. 2002;
131 Smith et al. 2008). The recent Terrain-Induced Rotor Experiment (T-REX) in March-April 2006
132 (Grubišić et al. 2008) was the first full research project to use the National Science Foundation
133 (NSF) – National Center for Atmospheric Research (NCAR) Gulfstream V (GV) (Laursen et al.
134 2006), which has better Global Positioning System (GPS) accuracy than the previous versions.
135 The National Aeronautics and Space Administration (NASA) high-altitude ER-2 research
136 aircraft was also employed during the recent Cirrus Regional Study of Tropical Anvils and
137 Cirrus Layers Florida Area Cirrus Experiment (CRYSTAL-FACE) (Jensen et al. 2004), which
138 conducted research flights in the vicinity of sub-tropical and tropical deep convection to study
139 the effects of convectively generated gravity waves (Wang et al. 2006). However, systematic *in-*
140 *situ* measurements of mesoscale gravity waves, especially those associated with upper-
141 tropospheric jet-front systems in the ExUTLS are very scarce. Relevant work includes Nastrom
142 and Fritts (1992) and Fritts and Nastrom (1992), who used commercial aircraft measurements to
143 infer the different sources of gravity waves (convections, front, topography, and jet streaks).
144 They found that mesoscale variances of horizontal wind and temperature were large at the jet-
145 front vicinity regions. However, little is known quantitatively about the generation mechanisms,
146 propagation and characteristics of gravity waves associated with the tropospheric jet streaks.
147 This is due in part to the fact that gravity waves are transient in nature and hard to resolve with
148 regular observing networks (Zhang et al. 2004).

149 The recent Stratosphere-Troposphere Analyses of Regional Transport 2008 (START08)
150 experiment was conducted to examine the chemical structure of the ExUTLS in relation to
151 dynamical processes spanning a range of scales (Pan et al. 2010). In particular, one specific goal

152 of START08 was to observe the properties of gravity waves generated by multiple sources,
153 including jets, fronts, and topography. During the START08 field campaign, a total of 18
154 research flight (RF) missions were carried out during April-June 2008 from the NCAR aviation
155 facility in Broomfield, Colorado (also see the online field catalog of the 18 RFs at
156 http://catalog.eol.ucar.edu/start_08/missions/missions.html). The second flight (RF02), which
157 occurred on 21-22 April 2008, was dedicated, to our knowledge for the first time, to probing
158 mesoscale gravity waves associated with a strong upper-tropospheric jet-front system, even
159 though some previous studies may have [recognized the presence of these waves](#) (e.g., Shapiro
160 and Kennedy 1975; Koch et al. 2005). Although only one flight specifically targeted gravity
161 waves, many of the other flights during START08 obtained high-quality observations of gravity
162 waves in the ExUTLS under a wide range of meteorological conditions. This study is an analysis
163 of the gravity wave observations from the START08 mission.

164 A brief description of the experimental design for RF02 and its corresponding
165 mesoscale simulation are presented in section 2, followed in section 3 by a review of the flight-
166 level measurements. Section 4 investigates the localized wave variance with wavelet analysis
167 and examines the polarization relationship based on cospectrum/quadr spectrum analysis.
168 Several examples of wave-like variances are shown and discussed in section 5. Section 6
169 contains a summary.

170

171 2. Experimental design

172 The GV research aircraft is ideally suited for investigating gravity waves in the ExUTLS
173 region. The flight ceiling of the aircraft is about 14 km with the START08 payload, which
174 enables sampling the vertical structure of the ExUTLS. With a typical flight speed of ~250 m/s at

Junhong Wei 5/27/2015 9:21 AM

Deleted: already measured or analyzed them

176 cruise altitude, the flight duration of ~8 hours for a single flight enables the GV to sample a large
177 geographic area with high-resolution (1-Hz) *in-situ* observations. A total of 68 flight segments
178 (color lines in Fig. 1) during the START08 are selected for analysis (also see Fig. 2 in Pan et al.
179 2010 for GV ground tracks of the 18 RFs). Each of these flight segments is longer than 200 km
180 and has near-constant flight-level static pressure and a relatively straight path. This will largely
181 eliminate spurious wave variance due to rapid changes in direction or altitude. In particular, the
182 RF02 mission was conducted over the central United States (38.87-51.10°N, 94.00-109.95°W) to
183 study the gravity wave excitation from a jet-front system and topography in the ExUTLS (Fig. 2
184 and Table 1). It started at 17:53 UTC on 21 April 2008 and finished at 02:54 UTC on 22 April
185 2008. This ~8-hour flight covered a total horizontal distance of ~6700 km, mostly in the lower
186 stratosphere. Five flight segments (thick blue lines in Fig. 1; thick blue lines in Fig. 2b-Fig. 2f;
187 details in section 3) in RF02 are used here. For most of the 5 flight segments, the aircraft flew at
188 an altitude of ~12.5 km (red lines in Fig. 3d; Table 1) and at a speed of ~250 ms⁻¹ (Table 1).

189 The Weather Research and Forecast (WRF) model (Skamarock et al. 2005) was used for
190 flight-planning forecasts. Real-time forecasts used WRF version 2.2.1 and were run with 45-km
191 and 15-km grid spacing for single deterministic forecasts (D1 and D2 in Fig. 1) and 45-km grid
192 spacing for ensemble prediction (D1 only). The model was initialized with a 30-member
193 mesoscale ensemble-based multi-physics data assimilation system (Zhang et al. 2006; Meng and
194 Zhang 2008a,b) and assimilated standard radiosonde observations. The real-time WRF forecasts
195 were archived at the START08 field catalog ([http://catalog.eol.ucar.edu/cgi-](http://catalog.eol.ucar.edu/cgi-bin/start08/model/index)
196 [bin/start08/model/index](http://catalog.eol.ucar.edu/cgi-bin/start08/model/index)). The flight track of RF02 was assigned to fly across the jet exit region
197 and gravity wave active area predicted by the real-time forecasts (also see Fig. 11 in Pan et al.
198 2010 for the real-time mesoscale forecast of gravity waves). Higher-resolution post-mission

199 WRF simulations with 5-km and 1.67-km grid spacing (D3 and D4 in Fig. 1) were also
200 conducted to examine the role of small-scale dynamical processes (e.g., convection and gravity
201 waves), which will be briefly reported in section 3. Nevertheless, an in-depth investigation of the
202 gravity wave dynamics based on the high-resolution post-mission WRF simulations is beyond
203 the scope of the current study, and will be reported elsewhere.

204

205 **3. Overview of the flight-level measurements**

206 Figure 2 depicts the track design of the entire flight and five flight segments during RF02,
207 along with the horizontal wind speed and the smoothed horizontal divergence near the flight
208 level simulated by the high-resolution post-mission WRF simulations valid at different
209 representative times of each five segments. Three flight segments pass mainly along an upper-
210 tropospheric jet streak. These are labeled J1, J2, and J3 and are displayed in Fig. 2b, 2c, and 2d,
211 respectively. Two other flight segments cross the mountains and high plains of Colorado and
212 Kansas. These are labeled M1 and M2 and are displayed in Fig. 2e and 2f, respectively. Flight
213 segment J3 is the longest during RF02. That segment includes flight through or above: the jet
214 core (gray shading in Fig. 2), a jet over high mountains (see the terrain map in Fig. 1), the exit
215 region of the jet, and a surface cold front (not shown). The other two segments, J1 and J2, were
216 intended to be a single segment, but an altitude change was necessary due to air traffic control.

217 Guided by the WRF model forecasts (e.g., Fig. 11 in Pan et al. 2010), this GV flight
218 mission sampled WRF-predicted gravity waves with different potential sources including
219 imbalance of jet streak and orographic forcing. Figure 3 shows the along-track horizontal
220 velocity component (u), across-track horizontal velocity component (v), horizontal wind speed
221 (V ; $V = \sqrt{u^2 + v^2}$), vertical velocity component (w), potential temperature (θ), corrected static

222 pressure (p_c), static pressure (p_s), hydrostatic pressure correction (p_h) derived from the airborne
223 *in-situ* measurements as well as flight height, and terrain along each of the five flight segments.
224 To facilitate spectral and wavelet analyses of these measurements, each variable from the 1-Hz
225 aircraft measurement along the flight segment is linearly interpolated into 250-m spatial series
226 with fixed resolution in distance. The right-hand rule is used to determine the relationships
227 among the positive along-track directions, the positive across-track directions, and the positive
228 vertical directions. For segments J1, J2, and J3, the positive along-track (across-track) directions
229 are all approximately toward the northeast (northwest). For segments M1 and M2, the positive
230 along-track (across-track) directions are both approximately toward the east (north). The
231 corrected static pressure p_c is calculated using the formula of Smith et al. (2008, their equation
232 12):

$$233 \quad p_c = p_s + p_h = p_s + \bar{\rho}g(z - z_{ref}) \quad (1)$$

234 where z is the GPS altitude, z_{ref} is the average altitude of flight segment and $\bar{\rho}$ is the average
235 density of flight segment. Corrected static pressure p_c from equation 1 is to correct the measured
236 static pressure p_s to a common height level (i.e., z_{ref}) based on the assumption of local
237 hydrostatic balance. Smith et al. (2008) suggests that the contribution of p_s to p_c is much smaller
238 than p_h , because it is assumed that the aircraft almost flies on an isobaric surface.

239 Consistent with what was predicted by the real time WRF forecast guidance (as shown in
240 Fig.11 of Pan et al. 2010) as well as simulated by the high-resolution post-mission WRF
241 simulations (in particular the horizontal divergence as potential signals of gravity waves as
242 shown in Fig. 2), the GV *in-situ* measurements of different atmospheric variables suggest there
243 are prevalent gravity wave activities along almost every leg of the 8-hr flight, most notably in the
244 vertical motion field. The largest amplitude of w (over 2 m/s) is during the middle portion of

Junhong Wei 5/27/2015 9:25 AM

Deleted: magnitude of above

246 segment J3 (location 680-780 km) on the lee slopes of the Rocky Mountains (also see the
247 discussion in section 5.2). The high terrain and the lee slopes also have the enhanced vertical
248 motions for both segment M1 and segment M2. Though not as large in amplitude, enhanced
249 fluctuations of vertical motions are also observed in the northern end of segment J3, which is in
250 the exit region of the upper-level jet streak and above the surface front. The enhanced variances
251 of vertical motion, accompanied by the changes in horizontal wind and potential temperature,
252 may be associated with topography for both M1 and M2 segments, even though the role of jet
253 cannot be isolated.

Junhong Wei 5/27/2015 9:28 AM

Deleted: on Figure 11

254 Power spectra of five selected aircraft measurement variables are given in Fig. 4 for each
255 of the five flight segments during RF02. The calculations of the spectra are performed with the
256 “specx_anal” function in the NCAR Command Language (NCL). Several steps are done before
257 the calculations. Firstly, the mean and least squares linear trend in each of the series are
258 removed. Secondly, smoothing by averaging 7 periodogram estimates is performed. Thirdly,
259 10% of the series are tapered. For segment J1, u , v , θ and p_c have several significant spectral
260 peaks for wavelengths ranging from 16-128 km (mesoscales). The statistically significant
261 spectral peaks in w are more for smaller scales, one at 2-4 km, and the other at 8-32 km. The
262 spectral characteristics for segment J2 are mostly the same as J1 except for much less power at
263 longer wavelengths (16-128 km) and only one peak at smaller scales (2-8 km). For segment J3,
264 both u and θ have statistically significant spectral peaks at mesoscales (~50 and 128 km) and at
265 smaller scales (8-16 km), the later (not the former) of which is also very pronounced for the w
266 spectrum. No significant spectral peak is found for the corrected static pressure p_c for segment
267 J3, except at 512 km, which is likely a reflection of the sub-synoptic scale pressure patterns at
268 the flight level (Fig. 2d). For segment M1, there is a significant mesoscale spectral peak at

Junhong Wei 5/27/2015 9:29 AM

Deleted: completely ruled out

Junhong Wei 5/27/2015 9:30 AM

Deleted: series

Junhong Wei 5/27/2015 9:31 AM

Deleted: perform the

273 around 32-64 km for u , θ and p_c , while smaller-scale variations from 4-16 km are also
274 significant for nearly all variables except for p_c . There are almost no significant spectral peaks
275 for all 5 variables for segment M2 except for around 2 km for w .

276 Past studies from both aircraft observations (e.g., Nastrom and Gage 1985; Bacmeister et
277 al. 1996; Lindborg 1999) and numerical simulations (e.g., Skamorcok 2004; Waite and Snyder
278 2013) have revealed/verified the existence of an approximate $-5/3$ power law that is expected for
279 the direct energy cascade in isotropic three-dimensional turbulence (e.g., Kolmogorov 1941) and
280 the inverse cascade in two dimensions (e.g., Kraichnan 1967), as well as an approximate -3
281 power law that is expected for quasigeostrophic turbulence theory (e.g., Charney 1971). The
282 spectral slopes of different variables derived from the flight-level measurements from START08
283 are thus examined here in detail. Overall in segment J3, the spectrum slope for θ (the third
284 column in Fig. 4d) is remarkably similar to those for u (the third column in Fig. 4a) and v (the
285 third column in Fig. 4b), except that there appears to be a deviation from both -3 and $-5/3$ power
286 laws for scales of $\sim 8\sim 16$ km. The spectral slope of w (the third column in Fig. 4c) is also similar
287 to that of θ (the third column in Fig. 4d) for all scales below 32 km, including the above-
288 mentioned deviation. However, for scale larger than ~ 32 km, the slope of w (the third column in
289 Fig. 4c) quickly dropped to almost zero, which is consistent with the continuity equation for
290 near-balanced non-divergent large-scale motions.

291 There are also similarities and differences in spectral slopes among different flight
292 segments depicted in Fig. 4. For example, the above-mentioned spectral shapes of u and v from
293 segment J3 are similar to those from segment J2 (i.e., the second and third columns in Fig. 4a
294 and Fig 4b). Such consistent signals probably result from sampling under similar large-scale
295 background flow at similar flight altitude with almost identical topography, especially between

296 the adjacent flight segments J1+J2 and J3. Despite the overall resemblance among the flight
297 segments of RF02, there are some unique characteristics in the power spectral distributions for
298 individual segments. For segments M1 and M2, for example, (i.e., the fourth column versus the
299 fifth column in Fig. 4), the slopes of u and v during segment M1 are approximately consistent
300 with a -3 power law for the scale of $\sim 0.5\sim 8$ km, while those during segment M2 follows a -5/3
301 power law instead. This is probably associated with the fact that segment M2 successfully
302 captures a rapid decrease in u (from ~ 65 m/s to ~ 40 m/s) while segment M1 has no such a
303 dramatic reduction in u (the fourth column in Fig. 3a versus the fifth column in Fig. 3a). Note
304 that the aircraft during segment M1 flew away from the jet core region, as the jet was still
305 moving eastward to the downhill side of the topography. In contrast, the aircraft during segment
306 M2 flew directly toward the approaching jet core at a lower flight level than segment M1 (the
307 fourth column in Fig. 3d versus the fifth column in Fig. 3d), and the observed decline of u (i.e., a
308 potential jet exit region) is located roughly on the downhill side of the topography (the fifth
309 column in Fig. 3d). This suggests that the spectral slopes for the aircraft measurements can, in
310 fact, be extremely sensitive to changes in the background flow, even though sampling takes place
311 in the same area only a few hours apart.

312 Figure 5 shows composite spectra for eight selected variables averaged over 68 flight
313 segments. Unsurprisingly, the composite spectra are much smoother due to averaging. For u
314 (Fig. 5a), v (Fig. 5b), and horizontal wind speed V (Fig. 5d), the slope of the power spectra are
315 consistent with a -5/3 power law for scales above $\sim 8\sim 16$ km. For w (Fig. 5c), its spectral slope
316 is generally consistent with -3 power laws for the scale of $\sim 0.5\sim 2$ km but is nearly zero for
317 scales over 32 km, while the slopes in between ($\sim 2\sim 32$ km) appear to follow an approximate -
318 5/3 power law, with a statistically significant spectral peak at $\sim 8\sim 16$ km. Even though the kinetic

319 energy spectra (Fig. 5e) may show a $-5/3$ slope that covers a larger range, the -3 slope over small
320 scale in KE is still evident. For θ (Fig. 5f) at scales between ~ 0.5 km and ~ 2 km, its slope also
321 obeys a -3 power law. For θ (Fig. 5f) at the scale greater than ~ 8 – ~ 16 km, the slope of power
322 spectrum tends to have a $-5/3$ slope, which is similar to u (Fig. 5a), v (Fig. 5b), and V (Fig. 5d)
323 for the same scales. For all the three pressure-related variables (i.e., p_c in Fig. 5g, p_s in Fig. 5h,
324 p_h in Fig. 5i), their slopes generally fall around a $-5/3$ power law, except for scales less than ~ 4
325 km in p_h (Fig. 5i). However, it is noteworthy that there is a sudden concavity (convexity) in p_c
326 (p_s or p_h) for scales between ~ 4 km and ~ 16 km (also see the discussion in section 5.3).

327

328 4. Wavelet analysis

329 4.1 Single-variable wavelet analysis

330 Standard spectral analysis methods characterize the variance as a function of wavelength
331 for an entire data record (flight segment), but do not indicate where variance of a particular
332 wavelength is located within the data record. We use wavelet analysis to complement the
333 spectral analysis in section 3 to study the variance as a function of wavelength within the five
334 flight segments from RF02. A Morlet wavelet function is employed in this study (e.g., Torrence
335 and Compo 1998; Zhang et al. 2001; Woods and Smith 2010). This is a continuous wavelet
336 transform that uses non-orthogonal complex wavelet functions comprising a plane wave
337 modulated by a Gaussian function (e.g., equation 1 in Torrence and Compo 1998):

$$338 \quad \psi_0(\eta) = \pi^{-1/4} e^{i\omega_0\eta} e^{-\eta^2/2} \quad (2)$$

339 where ω_0 is the dimensionless wave number and η is the dimensionless distance. Here ω_0 is set
340 to 6 to satisfy the admissibility condition (Farge 1992). The continuous wavelet transform, used

341 to extract localized spectral information, is defined as the convolution of the series of interest x
342 with the complex conjugate of the wavelet (e.g., equation 2 in Torrence and Compo 1998)

343
$$W_n(s) = \sum_{n'=0}^{N-1} x_{n'} \psi^* \left[\frac{(n'-n)\Delta x}{s} \right] \quad (3)$$

344 where ψ^* is the complex conjugate, n is the localized position index, s is the wavelet scale, and
345 Δx is the resolution of the data (0.25 km in this case). The cone of influence (COI) shows the
346 region of the wavelet spectrum where the edge errors cannot be ignored. Computation of the
347 wavelet spectrum and edge error is performed with the wavelet function of equation 3 (Torrence
348 and Compo 1998) in NCL.

349 Figure 6 contains the wavelet power spectra of five selected observed variables along the
350 five selected flight segments of RF02. Using the long segment J3 as an example again (third
351 column in Fig. 6), there is a substantial peak in the power of u (Fig. 6a) at wavelengths around
352 128-km between 400 and 700 km along the flight leg (also seen in p_c of Fig. 6e); \sim 100-km wave
353 power peaks at location 100-300 km; the wave power of wavelength from \sim 64 km to \sim 128 km
354 also peaks at location 1200-1400 km. The greatest similarity is between the spectra of w and θ
355 (Figs. 6c and d). For example, from location 100 km to 800 km during segment J3, local
356 maximum of power in w (the third column in Fig. 6c) resembles the one in θ (the third column
357 in Fig. 6d). In particular, three distinguished wave modes (\sim 64 km, \sim 32 km, and \sim 10 km in
358 along-track wavelength) collocate at location 600-800 km (downstream of a localized hill around
359 600 km in the third column of Fig. 3d). Relatively persistent \sim 10-km waves in w are shown at
360 location 200-700 km, which corresponds to a similar peak in the spectral analysis of w in the
361 third column of Fig. 4c. Note that such \sim 10-km waves are also found in other flight segments in
362 RF02 (e.g., location 0-600 km during segment M1, the fourth column in Fig. 6c) and other

363 research flights in START08 (not shown). Interpretations of such small-scale localized wave
364 | variances, as well as mesoscale localized wave variances, are discussed in section 5.

365

366 4.2 Polarization relationships from cross-wavelet analysis

367 Following Woods and Smith (2010), the phase relationship between two variables (e.g., u
368 and v , hereafter in short noted as $(u'v')_p$) can be determined from the cospectrum $(u'v')_c$ and
369 quadrature spectrum $(u'v')_q$, which are defined as (also see section 6c in Torrence and Compo
370 1998; equation 8 and appendix A in Woods and Smith 2010):

$$371 \quad (u'v')_c = \text{Re}\{U_n(s_j)V_n^*(s_j)\} \quad (4)$$

$$372 \quad (u'v')_q = \text{Im}\{U_n(s_j)V_n^*(s_j)\} \quad (5)$$

373 where U_n and V_n represent the wavelet transforms of u and v from equation 3, $U_n(s_j)V_n^*(s_j)$ is
374 the complex-valued cross-wavelet spectrum, while $\text{Re}\{ \}$ and $\text{Im}\{ \}$ represent the real and
375 imaginary parts of the variables inside the parentheses, respectively. Woods and Smith (2010)
376 focus on the energy flux by analyzing $(p_c'w')_c$ from equation 4 for vertically propagating waves
377 and $(p_c'w')_q$ from equation 5 for vertically trapped/ducted waves. In principle, $(p_c'w')_p$ should
378 be, theoretically speaking, associated with $(u'w')_p$ ($(v'w')_p$) (e.g., Eliassen and Palm 1960;
379 Lindzen 1990). This is particularly true for stationary mountain waves, which may be present for
380 RF02 given complex topography during each of the flight segments. However, in practice,
381 Woods and Smith (2010, their section 7) argued that the perturbation longitudinal velocity was
382 noisier than pressure in their study. In addition to equation 4 and equation 5, one can also define
383 the absolute coherence phase angle as $\frac{180}{\pi} \times \arctan\left(\frac{\text{Im}\{U_n(s_j)V_n^*(s_j)\}}{\text{Re}\{U_n(s_j)V_n^*(s_j)\}}\right)$ (also see section 6d in
384 Torrence and Compo 1998).

385 The phase relations among multiple variables are examined to further explore whether the
386 enhanced variances from the spectral and wavelet analyses are vertically propagating gravity
387 waves. Figure 7 shows three selected examples of cospectrum analysis (i.e., $(u'w')_c$ in Fig. 7a,
388 $(v'w')_c$ in Fig. 7b, $(p_c'w')_c$ in Fig. 7c), one selected example of quadrature spectrum analysis
389 (i.e., $(\theta'w')_q$ in Fig. 7d), and one example of absolute coherence phase angle for $(\theta'w')_p$ (Fig.
390 7e). In the case of a single monochromatic internal gravity wave propagating vertically, for
391 $(u'w')_c$ (Fig. 7a), positive (negative) values indicate upward (downward) flux of along-track
392 momentum. For $(v'w')_c$ (Fig. 7b), positive (negative) values indicate upward (downward) flux
393 of across-track momentum. For $(p_c'w')_c$ (Fig. 7c), positive (negative) values indicate positive
394 (negative) vertical energy transport. For the quadrature spectrum of $(\theta'w')_q$ (Fig. 7d), values
395 should be nonzero while the absolute coherence phase angle of $(\theta'w')_p$ (Fig. 7e) should be close
396 to 90 degree.

397 We again take segment J3 as an example (the third column in Fig. 7): for the small-scale
398 component with along-track wavelength less than 50 km (horizontal solid line), enhanced but
399 incoherent variances are detected for location 100-500 km and for location 600-800 km, with
400 fluctuating positive and negative values for both $(u'w')_c$ (the third column in Fig. 7a) and
401 $(v'w')_c$ (the third column in Fig. 7b). The variations in the signs of vertical transports of
402 horizontal momentum fluxes imply that this flight segment is sampling waves propagating in
403 both forward and backward direction, assuming the vertical energy transports are generally
404 upward. Correspondingly, the absolute coherence phase angle for $(u'v')_p$ (not shown) also
405 alternates frequently between nearly 0 degree and nearly 90 degree. In particular, some of the
406 enhanced variances in the cospectra for along-track wavelengths from ~4 km to ~16 km, though
407 fluctuating in signs, are significant above the 95% confidence level.

408 For the mesoscale component with wavelengths from ~50 to ~100 km, remarkable
409 localized quadrature variance is found in $(\theta'w')_q$ (the third column in Fig. 7d) for location 500-
410 800 km, consistent with the wavelet analysis of w in the third column of Fig. 6c and θ in the
411 third column of Fig 6d. The absolute coherence phase angle for $(\theta'w')_p$ in Fig. 7e also
412 demonstrate that the cross-wavelet spectrum between θ and w is mostly dominated by their
413 quadrature spectrum (red color shading in Fig. 7e), though there are some exceptions (blue color
414 shading in Fig. 7e).

415 The similarities/discrepancies among different wavelet cospectra and quadrature spectra
416 examined in Fig. 7 demonstrate the difficulties in gravity wave identification and the
417 uncertainties in gravity wave characteristics estimation based solely on aircraft measurements.

418 In addition to cross-wavelet analysis, the signs of the net fluxes (e.g., $\overline{u'w'}$, $\overline{v'w'}$, and
419 $\overline{w'p_c'}$) at each wavelength can also be estimated by the cospectrum analysis based on Fourier
420 transform over the entire segment (not shown). Generally speaking, for the scale below ~32 km,
421 both positive values and negative values are important in $\overline{u'w'}$ and $\overline{v'w'}$, while positive $\overline{w'p_c'}$
422 appears to be more continuous than negative $\overline{w'p_c'}$. For the scale above ~32 km, negative $\overline{u'w'}$
423 (positive $\overline{w'p_c'}$) appears to be more continuous than positive $\overline{u'w'}$ (negative $\overline{w'p_c'}$), while there
424 is no dominant sign for $\overline{v'w'}$ one way or the other.

426 5. Selected Wave-like Examples: signal of gravity waves or measurement noise?

427 This section examines several examples of wave-like variations during segment J3 in
428 more detail. Bandpass-filtered values of selected variables are computed by synthesizing the

Junhong Wei 5/27/2015 9:43 AM

Deleted: determined

Junhong Wei 5/27/2015 9:45 AM

Deleted: the

Junhong Wei 5/27/2015 9:45 AM

Deleted: s

Junhong Wei 5/27/2015 9:49 AM

Deleted: in

Junhong Wei 5/27/2015 9:45 AM

Deleted: are inconclusive

434 wavelet transform using wavelets with scales between j_1 and j_2 using (e.g., equation 29 in
 435 Torrence and Compo 1998)

$$436 \quad x_n' = \frac{\Delta j \Delta x^{1/2}}{C_\delta \psi_0(0)} \sum_{j=j_1}^{j_2} \frac{\text{Re}\{W_n(s_j)\}}{s_j^{1/2}} \quad (6)$$

437 where Δj is the scale resolution and C_δ is a reconstruction factor taken as 0.776 for Morlet
 438 wavelet. The wavelet-based filter in equation 6 has the advantage in removing noise at each
 439 wave number and isolating single events with a broad power spectrum or multiple events with
 440 different wave number (Donoho and Johnstone 1994; Torrence and Compo 1998).

441 Nine pairs of variables, including $(u'w')_p$, $(v'w')_p$, $(u'v')_p$, $(p_c'u')_p$, $(p_c'v')_p$,
 442 $(p_c'w')_p$, $(\theta'w')_p$, $(p_s'w')_p$, and $(p_h'w')_p$, are selected to examine whether the phase
 443 relationship of the variations in the airborne measurements is consistent with the linear theory for
 444 gravity waves. Generally speaking, the phase relation between two variables can be classified
 445 into two major categories: 1) In-phase or out-of-phase relationships, in which one variable leads
 446 or lags the other variable by approximately 0° or 180° ; 2) Quadrature relationships, in which one
 447 variable leads or lags the other by approximately 90° .

448 The phase relationships for linear gravity waves are determined by theory and their
 449 propagation characteristics. Take $(u'w')_p$, $(v'w')_p$, and $(p_c'w')_p$ as examples, if they have an
 450 in- or out-of-phase relationship, the waves are propagating in the vertical direction; if they have a
 451 quadrature relationship, the waves do not propagate vertically and may be trapped or ducted.
 452 Take $(u'v')_p$ as another example, if they have an in- or out-of-phase relationship, the waves may
 453 be internal gravity waves whose intrinsic frequencies are much higher than the Coriolis
 454 frequency; if they have a quadrature relationship, the waves may be inertio-gravity waves with
 455 intrinsic frequencies close to the Coriolis frequency. For vertically propagating linear gravity
 456 waves, $(\theta'w')_p$ should have a quadrature relationship. According to Smith et al. (2008), p_h'

457 should dominate over p_s' , if the aircraft almost flies on a constant pressure surface.
458 Consequently, $(p_h'w')_p$ should be almost identical to $(p_c'w')_p$.

459

460 5.1 Examples of mesoscale wave variances

461 Figure 8 demonstrates an example of potential mesoscale gravity waves selected based on
462 the wavelet analysis of u (Fig. 6a), w (Fig. 6c), θ (Fig. 6d), and p_c (Fig. 6e) for location 250-360
463 km in segment J3 (the exit region of northwesterly jet in Fig. 2d). The wave signals are further
464 highlighted by applying a wavelet-based filter (i.e., equation 6) to extract wavelike variations
465 with along-track wavelength between 100 and 120 km. Panels a, b, d, and e show out-of-phase
466 relationships for $(u'w')_p$, $(v'w')_p$, $(p_c'u')_p$, and $(p_c'v')_p$ respectively; while panels c, f, and i
467 show in-phase relationships for $(u'v')_p$, $(p_c'w')_p$, and $(p_h'w')_p$. Panels g and h show
468 quadrature relationships for $(\theta'w')_p$ and $(p_s'w')_p$. The observed phase relations shown in Fig. 8
469 are generally consistent with linear theory for propagating monochromatic gravity waves, as
470 indicated by the cospectrum/quadrature spectrum analysis in Fig. 7. These signals are likely to be
471 internal gravity waves (due to the in-phase relation of $(u'v')_p$ in Fig. 8c) with positive vertical
472 group velocity (due to their positive vertical energy flux, Fig. 8f).

473 In contrast, Figure 9 is an example of wave-like disturbances that lacks a clear,
474 propagating, linear-wave, phase relationship. This example is also selected based on the wavelet
475 analysis of segment J3 for u , v , and p_c (Figs. 6a, b, and e) for along-track wavelength near 128
476 km and location between 560 and 688 km along the segment. This segment lies above the
477 complex topography as depicted in the third column of Fig. 3d. According to Figs. 9a-9e,
478 $(u'w')_p$, $(u'v')_p$, and $(p_c'u')_p$ seem to have out-of-phase relationships, while $(v'w')_p$ and
479 $(p_c'v')_p$ have almost perfect in-phase relationships. These phase relationships appear to be

480 reasonable and generally consistent with the linear theory. The near in-phase relationship
481 exhibited by $(\theta'w')_p$ (Fig. 9g), however, raises doubts about whether these variations are true
482 gravity waves, as this is not consistent with linear theory. If they are in fact gravity wave signals,
483 the discrepancy highlights the difficulties of extracting gravity wave perturbations from
484 observations. For example, the mesoscale variances may be contaminated by small-scale
485 variability of θ and w due to the coexistence of wave variances at different scales for this region
486 (see the wavelet analysis of w in Fig. 6c in and θ in Fig. 6d). Additionally, there are uncertainties
487 in extracting mesoscale gravity waves from a varying background flow (e.g., Zhang et al. 2004),
488 especially for u , v and θ . Note that θ and w have a very consistent quadrature relation from ~ 8
489 km to ~ 64 km for this region in their quadrature spectrum of Fig. 7d (also see Fig. 7e), but this
490 quadrature relation (the third column in Fig. 7d), including their corresponding wavelet spectrum
491 (the third column in Fig. 6c and Fig. 6d) is much weaker for wavelengths near 128 km for
492 location 560-688 km in segment J3.

493 Consistent with Smith et al. (2008), the amplitude of p_h' is much larger than the
494 amplitude of p_s' for both examples of mesoscale wave variances. Therefore, $(p_h'w')_p$ is almost
495 identical to $(p_c'w')_p$ for both cases (Fig. 8f versus Fig. 8i; Fig. 9f versus Fig. 9i). It appears that
496 the assumption of constant p_s flight height is valid for these two mesoscale examples.

497

498 *5.2 Examples of small-scale wavelike variations*

499 Figure 10 shows an example of short-scale wave-like disturbances that have a phase
500 relationship consistent with linear gravity wave theory based on the wavelet analysis in Fig. 6
501 with scales from 32 to 64 km located at 650 to 750 km during segment J3. In-phase relationships
502 are seen in the filtered signals of $(p_c'v')_p$ (Fig. 10e), while out-of-phase relationships are seen in

503 $(u'v')_p$ and $(p_c'u')_p$ (Figs. 10c and d). Quadrature relationships can generally be seen in
504 $(u'w')_p$, $(v'w')_p$, $(p_c'w')_p$, and $(\theta'w')_p$ (Figs. 10a, b, f, and g). These small-scale waves have
505 no apparent vertical flux of horizontal momentum (Figs. 10a and b) and no vertical energy flux
506 (Fig. 10f), a key sign of vertically trapped gravity waves. Short-scale waves based on GV aircraft
507 measurements and/or numerical simulations are also discussed in Smith et al. (2008), Woods and
508 Smith (2010; 2011).

509 However, parts of the small-scale wave variations derived from the *in-situ* measurements,
510 especially for wavelengths from 5 to 15 km, may be difficult to classify as gravity waves. Figure
511 11 shows an example of short-scale wave variations in the aircraft measurements with along-
512 track wavelengths from 8 to 16 km for locations 680 to 780 km along segment J3. As depicted in
513 Fig. 11, $(u'w')_p$ (Fig. 11a) appears to have a quadrature relationship, even though this relative
514 phase varies, especially for locations from 710 to 730 km. Compared to $(u'w')_p$ (Fig. 11a),
515 $(v'w')_p$ and $(\theta'w')_p$ (Fig. 11b and g) have consistent quadrature relationships within this 100-
516 km distance. On the other hand, $(u'v')_p$ (Fig. 11c) varies significantly from one wavelength to
517 the next. The amplitude of w' in this example is extremely large (~ 2.5 m/s at its maximum) in
518 this selected example. In comparison, the amplitude of p_c' is rather small, and it is actually too
519 small to be noticed when using a wider bandpass window (not shown). Also, the quadrature
520 relationship in $(p_c'w')_p$ (Fig. 11f) is not as remarkable as those in $(u'w')_p$ and $(v'w')_p$ (Figs.
521 11a and b), which appears to contradict the theoretical description of Eliassen and Palm (1960)
522 on energy and momentum fluxes (also see Lindzen 1990). In addition, it is worth mentioning that
523 $(p_s'w')_p$ and $(p_h'w')_p$ in Figs. 11h and i have almost perfect out-of-phase and in-phase
524 relationships, respectively.

525 In contradiction to Smith et al. (2008), the amplitude of p_h' in the above example of Fig.
 526 11 is comparable with the amplitude of p_s' (Fig. 11h versus Fig. 11i). Surprisingly, $(p_c'w')_p$,
 527 $(p_s'w')_p$, and $(p_h'w')_p$ are also very different from each other (compare Figs. 11f, h, and i). The
 528 signals of p_s' and p_h' (Fig. 11h and i) are out-of-phase for wavelengths near 10 km and have
 529 comparable amplitude, which leads to nearly no such wave variances in p_c' (Fig. 11d-11f) given
 530 p_c' is the sum of p_s' and p_h' .

531

532 *5.3 Insight from spectral analysis of different pressure variables*

533 Figure 12a compares the power spectrum of three pressure-related variables (i.e.,
 534 corrected static pressure p_c , static pressure p_s , hydrostatic pressure correction p_h ; also see
 535 equation 1). Using segment J3 as an example, for wavelengths greater than ~ 32 km, p_c is almost
 536 identical to p_h ; for wavelengths between ~ 32 km and ~ 4 km, the variances between p_s and p_h
 537 are comparable, and the variances of p_c are noticeably smaller than those in p_s and p_h ; for
 538 wavelengths less than ~ 4 km, p_c is almost identical to p_s . Figure 12b shows the quantity

539 $\sqrt{\frac{spec(p_s)+spec(p_h)}{spec(p_c)}}$, where $spec()$ indicates the power spectrum of the variable inside the

540 parentheses (e.g., Figs. 4-5). For segment J3, the square root of the ratio is close to 1.0 for the
 541 wavelengths greater than ~ 32 km and less than ~ 4 km. At intermediate wavelengths, the square
 542 root of the ratio reaches a maximum near 10 for wavelengths of ~ 10 km. This suggests that p_s'
 543 and p_h' may tend to cancel each other at intermediate scales, which reduces the amplitude of p_c'
 544 at these intermediate wavelengths (also see the example in Fig. 11) since p_c' is the sum of p_s'
 545 and p_h' . Similar behaviors can be also observed in other segments, although the exact ranges of
 546 the intermediate wavelengths may be different from case to case.

547 Figure 12 suggests that the assumption of constant p_s flight height may not be valid at all
548 scales, though it appears to be true for mesoscale waves. In consequence, p_h' may not always
549 dominate over p_s' as assumed in Smith et al. (2008). The spectral analysis and wavelet analysis
550 of p_s (not shown) demonstrate that p_s indeed has relatively large variances for the short-scale
551 range, and that p_s and w share some common characteristics (also see Fig. 3). Moreover, the
552 hydrostatic approximation, which is the underlying assumption for equation 1, may no longer be
553 valid for short scales.

554

555 6. Concluding remarks and discussion

556 One of the primary objectives of the recent START08 field experiment is to characterize
557 the sources and impacts of mesoscale waves with high-resolution flight-level aircraft
558 measurements and mesoscale models. The current study focuses on the second research flight
559 (RF02), which was the first airborne mission dedicated to probing gravity waves associated with
560 strong upper-tropospheric jet-front systems and high topography. Based on spectral and wavelet
561 analyses of the *in-situ* observations, along with a diagnosis of the polarization relationships, it is
562 found that there are clear signals of significant mesoscale variations with wavelengths ranging
563 from ~50 to ~500 km in almost every segment of the 8-hr flight (order ranging from 0.01 m/s to
564 1.0 m/s in vertical motion), which took place mostly in the lower stratosphere. The flow sampled
565 by the aircraft covers a wide range of background conditions including near the jet core, a jet
566 over the high mountains, and the exit region of the jet. ~~There is clear evidence of vertically~~
567 ~~propagating gravity waves of along-track wavelengths between 100 and 120 km during some of~~
568 ~~the flight segments. There are also some indications of potential vertically trapped gravity waves~~
569 ~~of along-track wavelengths between 32 and 64 km.~~

Fuqing Zhang 5/27/2015 10:05 AM

Deleted: Among the positive findings

Fuqing Zhang 5/27/2015 10:06 AM

Deleted: is

Fuqing Zhang 5/27/2015 10:08 AM

Deleted: , as well as evidence of

573 A general summary of power spectra is as follows: (1) Horizontal velocity components
574 and potential temperature for the scale approximately between ~8 km and ~256 km display the
575 approximate -5/3 power law. The common characteristics and individual features of the wave
576 variances and spectrum slope behaviors appear to be generally consistent with past studies on the
577 spectral analysis of aircraft measurements, including Nastrom and Gage (1985) using the Global
578 Atmospheric Sampling Program (GASP) flight dataset, and Lindborg (1999) using the
579 Measurement of Ozone and Water Vapor by Airbus In-Service Aircraft (MOZAIC) aircraft
580 observations. In addition, our recent separate study of idealized moist baroclinic waves (Sun and
581 Zhang 2015) suggests that the presence of moist convection and mesoscale gravity waves,
582 though probably non-isotropic, does appear to steer the mesoscale range of the spectral slope to
583 be -5/3. (2) Vertical velocity component appears to be flat approximately within the range
584 between ~8 km and ~256 km. (3) The power spectra of horizontal velocity components and
585 potential temperature roll over to a -3 power law for the scale between ~0.5 km and ~8 km.
586 Based on three aircraft campaign projects, Bacmeister et al. (1996) has also reported the small-
587 scale steepening behavior. The characteristics in (3) are generally observed except (4) when this
588 part of the spectrum is activated, as recorded ~~clearly~~ by M2, one of the highlighted flight
589 segments. Interestingly, the M1 segment immediately prior to the M2 segment did not record the
590 event, probably due to the fast changing background flow. Spectral behaviors of atmospheric
591 variables have also been studied by high-resolution non-hydrostatic mesoscale numerical
592 weather prediction (NWP) models (e.g., Skamarock 2004; Tan et al. 2004; Zhang et al. 2007;
593 Waite and Snyder 2013; Bei and Zhang 2014).

594 Smaller-scale wavelike oscillations below 50 km are found to be quite transient. In
595 particular, aircraft measurements of several flight segments are dominated by signals with

Fuqing Zhang 5/27/2015 10:11 AM
Deleted: beautifully

Junhong Wei 5/23/2015 7:35 PM
Deleted: In contrast,

Junhong Wei 5/23/2015 7:35 PM
Deleted: s

599 sampled periods of ~20~60 seconds and wavelengths of ~5~15 km (assuming that the typical
600 flight speed is approximately 250 m/s). This study suggests that at least part of the nearly-
601 periodic high-frequency signals might be unphysical and a result of intrinsic observational errors
602 in the aircraft measurements or small-scale flight-altitude fluctuations that are difficult to account
603 for. Such potentially contaminated variations are often collocated with larger-scale wave signals,
604 which in turn may lead to larger uncertainties in the estimation of the wave characteristics. Part
605 of the uncertainties may come from the inability of the aircraft to maintain constant static
606 pressure altitude in the presence of small-scale turbulence. The current study mainly [focuses on](#)
607 [examining the](#) fluctuations with the use of linear theory for monochromatic gravity waves.
608 Therefore, in addition to measurement errors, the possibilities that those fluctuations may be due
609 to other physical phenomena (e.g., nonlinear dynamics, shear instability and/or turbulence)
610 cannot be completely ruled out [in the current study](#).

611 Although the real-time mesoscale analysis and prediction system gave a reasonable
612 forecast guidance on the region of potential gravity wave activities, it remains to be explored (1)
613 how well the current generation of numerical weather models predicts the excitation of gravity
614 waves, (2) how often gravity waves break in the ExUTLS region, and (3) what evidence in tracer
615 measurements is shown for the contribution of gravity wave breaking to mixing. Future work
616 will also seek to examine the origin and dynamics of the gravity waves observed during RF02 of
617 START08 through a combination of observations and numerical modeling. This will help to
618 distinguish whether the sampled mesoscale and small-scale variances are gravity waves or
619 artifacts of the observing system. [In addition, under the idealized controllable atmosphere with](#)
620 [varying degrees of convective instability and baroclinic instability \(e.g., Zhang 2004; Wang and](#)
621 [Zhang 2007; Wei and Zhang 2014; Sun and Zhang 2015\), high-resolution simulations of](#)

Junhong Wei 5/23/2015 4:58 PM

Deleted: -

Junhong Wei 5/27/2015 9:57 AM

Deleted: attempts to verify

Junhong Wei 5/23/2015 7:37 PM

Deleted: Nevertheless, despite the presence of possibly spurious wave oscillations in different flight segments, the power spectra of horizontal winds and temperature averaged over many START08 flight segments generally follow the -5/3 power law. The common characteristics and individual features of the wave variances and spectrum slope behaviors appear to be generally consistent with past studies on the spectral analysis of aircraft measurement, including Nastrom and Gage (1985) using the Global Atmospheric Sampling Program (GASP) flight dataset, and Lindborg (1999) using the Measurement of Ozone and Water Vapor by Airbus In-Service Aircraft (MOZAIC) aircraft observations. Spectral behaviors of atmospheric variables have also been studied by high-resolution non-hydrostatic mesoscale numerical weather prediction (NWP) models (e.g., Skamarock 2004; Tan et al. 2004; Zhang et al. 2007; Waite and Snyder 2013; Bei and Zhang 2014).

646 [baroclinic jet/front systems will be employed to understand \(1\) how to constrain the](#)
647 [parameterizations of jet/front gravity waves in general circulation models, \(2\) the role of gravity](#)
648 [waves in mesoscale predictability, and \(3\) the contribution of gravity waves to mesoscale energy](#)
649 [spectra in global wavenumber distribution or in multi-dimensional wavenumber distribution.](#)

Junhong Wei 5/23/2015 8:10 PM

Formatted: Font:Not Italic

651 **Acknowledgments:** The START08 experiment is sponsored by the National Science Foundation
652 (NSF). A large number of people contributed to the success of START08 experiment. The
653 dedication of the instrument team, co-sponsored by NCAR, University of Colorado, Harvard
654 University, University of Miami, Princeton University, NOAA Earth System Research
655 Laboratory (ESRL) Global Monitoring Division (GMD) and Chemical Science Division (CSD),
656 and the NCAR Research Aviation Facility staff in running the flight operation are the key factors
657 in the success of campaign. We also acknowledge the effort and skill of the GV pilots Henry
658 Boynton and Ed Ringleman, which was critical to meeting mission objectives. We benefit from

659 [review comments from the editor Tim Dunkerton and four anonymous reviewers on an earlier](#)
660 [versions](#) of the manuscript. This research is sponsored by NSF grants 0618662, 0722225,
661 0904635, and 1114849. [Computing is performed at the Texas Advanced Computing Center](#)
662 [\(TACC\).](#)

Fuqing Zhang 5/27/2015 10:12 AM

Deleted: initial

Junhong Wei 5/27/2015 9:01 AM

Deleted: three

665 **References**

- 666 Alexander, M. J., and K. H. Rosenlof, 2003: Gravity-wave forcing in the stratosphere:
667 Observational constraints from the Upper Atmosphere Research Satellite and implications for
668 parameterization in global models. *J. Geophys. Res. – Atmos.*, 108: Art. No. 4597.
- 669 Bacmeister, J. T., S. D. Eckermann, P. A. Newman, L. Lait, K. R. Chan, M. Loewenstein, M. H.
670 Proffitt, and B. L. Gary, 1996: Stratospheric horizontal wavenumber spectra of winds, po-
671 tential temperature, and atmospheric tracers observed by high-altitude aircraft. *J. Geophys.*
672 *Res.*, 101, 9441–9470.
- 673 Bei, N., and F. Zhang, 2014: Mesoscale Predictability of Moist Baroclinic Waves: Variable and
674 Scale Dependent Error Growth. *Advances in Atmospheric Sciences*, doi: 10.1007/s00376-
675 014-3191-7.
- 676 Bertin F., Campistron B., Caccia J. L., Wilson R., 2001: Mixing processes in a tropopause
677 folding observed by a network of ST radar and lidar. *Annales Geophysicae*, 19, 953-963.
- 678 Bosart, L. F., W. E. Bracken, and A. Seimon, 1998: A study of cyclone mesoscale structure with
679 emphasis on a large-amplitude inertia-gravity waves. *Mon. Wea. Rev.*, 126, 1497-1527.
- 680 Brown, P. R. A., 1983: Aircraft measurements of mountain waves and their associated
681 momentum flux over the british isles. *Q. J. R. Meteorol. Soc.*, 109, 849-865.
- 682 Charney, J. G., 1971: Geostrophic turbulence. *J. Atmos. Sci.*, 28, 1087–1095.
- 683 Donoho, D. L., and I. M. Johnstone, 1994: Ideal spatial adaptation by wavelet shrinkage.
684 *Biometrika*, 81, 425–455.
- 685 Dornbrack, A., T. Birner, A. Fix, H. Flentje, A. Meister, H. Schmid, E. V. Browell, and M.
686 J. Mahoney, 2002: Evidence for inertia gravity waves forming polar stratospheric clouds
687 over scandinavia. *J. Geophys. Res.*, 107, 8287, doi:10.1029/2001JD000452.

688 Doyle, J., H. Volkert, A. Dornbrack, K. Hoinka, and T. Hogan, 2002: Aircraft measurements and
689 numerical simulations of mountain waves over the central Alps: A pre-MAP test case. *Q. J.
690 R. Meteorol. Soc.*, 128, 2175-2184.

691 Einaudi, F., A. J. Bedard, and J. J. Finnigan, 1989: A climatology of gravity waves and other
692 coherent disturbances at the Boulder Atmospheric Observatory during March–April 1984. *J.
693 Atmos. Sci.*, 46, 303–329.

694 Eliassen, A. and E. Palm, 1960: On the transfer of energy in stationary mountain waves. *Geophys.
695 Publ.*, 22, 1-23.

696 Farge, M., 1992: Wavelet transforms and their applications to turbulence. *Annu. Rev. Fluid
697 Mech.*, 24, 395-457.

698 Fritts, D. C., and G. D. Nastrom, 1992: Sources of mesoscale variability of gravity waves. Part
699 II: Frontal, convective, and jet stream excitation. *J. Atmos. Sci.*, 49, 111-127.

700 Gong, J., and M. A. Geller, 2010: Vertical fluctuation energy in United States high vertical
701 resolution radiosonde data as an indicator of convective gravity wave sources. *J. Geophys.
702 Res.* 115 (D11): 10.1029/2009JD012265.

703 Grivet-Talocia, S., F. Einaudi, W. L. Clark, R. D. Dennett, G. D. Nastrom, and T. E. VanZandt,
704 1999: A 4-yr Climatology of Pressure Disturbances Using a Barometer Network in Central
705 Illinois. *Mon. Wea. Rev.*, 127, 1613–1629.

706 Grubišić, V., J.D. Doyle, J. Kuettner, S. Mobbs, R.B. Smith, C.D. Whiteman, R. Dirks, S.
707 Czyzyk, S.A. Cohn, S. Vosper, M. Weissmann, S. Haimov, S.F.J. De Wekker, L.L. Pan, and
708 F.K. Chow, 2008: The Terrain-Induced Rotor Experiment. *Bull. Amer. Meteor. Soc.*, 89,
709 1513–1533.

710 Hertzog, A., and F. Vial, 2001: A study of the dynamics of the equatorial lower stratosphere by
711 use of ultra-long-duration balloons: 2. Gravity waves. *J. Geophys. Res.*, 106, 22 745– 22 761.

712 Jensen, E. J., D. Starr, and O. B. Toon, 2004: Mission investigates tropical cirrus clouds. *EOS*,
713 85, 45-50.

714 Kaplan, M. L., S. E. Koch, Y.-L. Lin, R. P. Weglarz, and R. A. Rozumalski, 1997: Numerical
715 simulations of a gravity wave event over CCOPE. Part I: The role of geostrophic adjustment
716 in mesoscale jetlet formation. *Mon. Wea. Rev.*, 125, 1185–1211.

717 Karacostas, T. S. and J. D. Marwitz, 1980: Turbulent kinetic energy budgets over
718 mountainousterrain. *J. Appl. Meteor.*, 19, 163-174.

719 Koch S.E., Jamison B.D., Lu C.G., Smith T.L., Tollerud E.I., Girz C., Wang N., Lane T.P.,
720 Shapiro M.A., Parrish D.D., Cooper O.R., 2005: Turbulence and gravity waves within an
721 upper-level front, *J. Atmos. Sci.*, 62, 3885-3908.

722 Koch, S. E., F. Zhang, M. Kaplan, Y.-L. Lin, R. Weglarz, and M. Trexler, 2001: Numerical
723 simulation of a gravity wave event observed during ccope. part 3: the role of a mountain-
724 plains solenoid in the generation of the second wave episode. *Mon. Wea. Rev.*, 129, 909–
725 932.

726 Kolmogorov, A. N., 1941: The local structure of turbulence in incompressible viscous fluid for
727 very large Reynolds number. *Dokl. Akad. Nauk SSSR*, 30, 301–305.

728 Koppel, L. L., L. F. Bosart, and D. Keyser, 2000: A 25-yr climatology of large-amplitude hourly
729 surface pressure changes over the conterminous United States. *Mon. Wea. Rev.*, 96, 51–68.

730 Kraichnan, R. H., 1967: Inertial ranges in two-dimensional turbulence. *Phys. Fluids*, 10, 1417–
731 1423.

732 Lane, T. P., J. D. Doyle, R. Plougonven, M. A. Shapiro, and R. D. Sharman, 2004: Ob-
733 servations and numerical simulations of inertia-gravity waves and shearing instabilities in the
734 vicinity of a jet stream. *J. Atmos. Sci.*, 61, 2692–2706.

735 Lane, T. P., M. J. Reeder, T. L. Clark, 2001: Numerical Modeling of Gravity Wave Generation
736 by Deep Tropical Convection. *J. Atmos. Sci.*, 58, 1249–1274.

737 Laursen, K. K., D. P. Jorgensen, G. P. Brasseur, S. L. Ustin, and J. R. Huning, 2006: HIAPER:
738 The next generation NSF/NCAR research aircraft. *Bull. Amer. Meteor. Soc.*, 87, 896-909.

739 Leutbecher, M. and H. Volkert, 2000: The propagation of mountain waves into the stratosphere:
740 Quantitative evaluation of three-dimensional simulations. *J. Atmos. Sci.*, 57, 3090-3108.

741 Lilly, D. K. and P. J. Kennedy, 1973: Observations of a stationary mountain wave and its
742 associated momentum flux and energy dissipation. *J. Atmos. Sci.*, 30, 1135-1152.

743 Lin, Y., and F. Zhang, 2008: Tracking gravity waves in baroclinic jet-front systems. *J. Atmos.*
744 *Sci.*, 65, 2402-2415.

745 Lindborg, E., 1999: Can the atmospheric kinetic energy spectrum be explained by two-
746 dimensional turbulence? *J. Fluid Mech.*, 388, 259 –288.

747 Lindzen, R. S., 1990: *Dynamics in Atmospheric Physics*. Cambridge University Press, 320 pp.

748 Meng, Z, and F. Zhang, 2008a: Test of an ensemble-Kalman filter for mesoscale and regional-
749 scale data assimilation. Part III: Comparison with 3Dvar in a real-data case study. *Mon. Wea.*
750 *Rev.*, 136, 522-540.

751 Meng, Z, and F. Zhang, 2008b: Test of an ensemble-Kalman filter for mesoscale and regional-
752 scale data assimilation. Part IV: Performance over a warm-season month of June 2003. *Mon.*
753 *Wea. Rev.*, 136, 3671-3682.

754 Mirzaei, M., C. Zülicke, A. Mohebalhojeh, F. Ahmadi-Givi, and R. Plougonven (2014),
755 Structure, energy, and parameterization of inertia-gravity waves in dry and moist simulations
756 of a baroclinic wave life cycle, *J. Atmos. Sci.*, 71, 2390–2414. doi:
757 <http://dx.doi.org/10.1175/JAS-D-13-075.1>

758 Moustou, M., H. Teitelbaum, P. F. J. van Velthoven, and H. Kelder, 1999: Analysis of gravity
759 waves during the POLINAT experiment and some consequences for stratosphere-troposphere
760 exchange. *J. Atmos. Sci.*, 56, 1019-1030.

761 Nastrom, G. D., and D. C. Fritts, 1992: Sources of mesoscale variability of gravity waves. Part I:
762 Topographic excitation. *J. Atmos. Sci.*, 49, 101–110.

763 Nastrom, G. D., and K. S. Gage, 1985: A Climatology of Atmospheric Wavenumber Spectra of
764 Wind and Temperature Observed by Commercial Aircraft. *J. Atmos. Sci.*, 42, 950–960.

765 O’Sullivan, D. and T. J. Dunkerton, 1995: Generation of inertia-gravity waves in a simulated life
766 cycle of baroclinic instability. *J. Atmos. Sci.*, 52, 3695–3716.

767 Pan, L. L., K. P. Bowman, E. L. Atlas, S. C. Wofsy, F. Zhang, and co-authors, 2010:
768 Stratosphere-Troposphere Analyses of Regional Transport Experiment. *Bulletin of the*
769 *American Meteorological Society*, 91, 327-342.

770 Pavelin E., J.A. Whiteway, G. Vaughan, 2001: Observation of gravity wave generation and
771 breaking in the lowermost stratosphere. *J. Geophys. Res.*, 106 (D6), 5173-5179.

772 Plougonven, R. and C. Snyder, 2007: Inertia-gravity waves spontaneously generated by jets and
773 fronts. Part I: Different baroclinic life cycles. *J. Atmos. Sci.*, 64, 2502–2520.

774 Plougonven, R., and F. Zhang, 2014: Internal gravity waves from atmospheric jets and fronts.
775 *Reviews of Geophysics*, 52, doi: 10.1002/2012RG000419.

776 Plougonven, R., H. Teitelbaum, and V. Zeitlin, 2003: Inertia gravity wave generation by
777 tropospheric midlatitude jet as given by the fronts and atlantic storm-track experiment radio
778 soundings. *J. Geophys. Res.-Atmos.*, 108, 888–889.

779 Pokrandt, P. J., G. J. Tripoli, and D. D. Houghton, 1996: Processes leading to the formation of
780 mesoscale waves in the midwest cyclone of 15 december 1987. *Mon. Wea. Rev.*, 124, 2726–
781 2752.

782 Poulos, G. S., William Blumen, David C. Fritts, Julie K. Lundquist, Jielun Sun, Sean P. Burns,
783 Carmen Nappo, Robert Banta, Rob Newsom, Joan Cuxart, Enric Terradellas, Ben Balsley,
784 and Michael Jensen, 2002: CASES-99: A Comprehensive Investigation of the Stable
785 Nocturnal Boundary Layer. *Bull. Amer. Meteor. Soc.*, 83, 555–581.

786 Powers, J. G. and R. J. Reed, 1993: Numerical model simulation of the large-amplitude
787 mesoscale gravity-wave event of 15 December 1987 in the central United States. *Mon. Wea.*
788 *Rev.*, 121, 2285–2308.

789 Radok, U., 1954: A procedure for studying mountain effects at low levels. *Bull. Amer. Meteor.*
790 *Soc.*, 35/9, 412.

791 Ramamurthy, M. K., R. M. Rauber, B. Collins, and N. K. Malhotra, 1993: A comparative study
792 of large-amplitude gravity-wave events. *Mon. Wea. Rev.*, 121, 2951–2974.

793 Rauber, R. M., M. Yang, M. K. Ramamurthy, and B. F. Jewett, 2001: Origin, evolution, and
794 fine-scale structure of the St. Valentine’s Day mesoscale gravity wave observed during
795 storm-fest. Part I: Origin and evolution. *Mon. Wea. Rev.*, 129, 198–217.

796 Reeder, M. J., and M. Griffiths, 1996: Stratospheric inertia-gravity waves generated in a
797 numerical model of frontogenesis. II: Wave sources, generation mechanisms and momentum
798 fluxes. *Quart. J. Roy. Meteor. Soc.*, 122, 1175–1195.

799 Schneider, R. S., 1990: Large-amplitude mesoscale wave disturbances within the intense
800 midwest extratropical cyclone of 15 December 1987. *Wea. Forecasting*, 5, 533–558.

801 Shapiro, M. A., and P. J. Kennedy, 1975: Aircraft Measurements of Wave Motions within
802 Frontal Zone Systems. *Mon. Wea. Rev.*, 103, 1050–1054. doi:
803 [http://dx.doi.org/10.1175/1520-0493\(1975\)103<1050:AMOWMW>2.0.CO;2](http://dx.doi.org/10.1175/1520-0493(1975)103<1050:AMOWMW>2.0.CO;2)

804 Skamarock, W. C., 2004: Evaluating Mesoscale NWP Models Using Kinetic Energy Spectra.
805 *Mon. Wea. Rev.*, 132, 3019–3032.

806 Skamarock, W. C., J. B. Klemp, J. Dudhia, D.O. Gill, D. M. Barker, W. Wang, and J. G. Powers,
807 2005: A description of the Advanced Research WRF Version 2. NCAR technical note
808 468+STR, 88 pp.

809 Smith, R. B., 1976: The generation of lee waves by the blue ridge. *J. Atmos. Sci.*, 33, 507-519.

810 Smith, R. B., 1980: Linear theory of stratified hydrostatic flow past an isolated mountain. *Tellus*,
811 348-364.

812 Smith, R. B., B. K. Woods, J. Jensen, W. A. Cooper, J. D. Doyle, Q. Jiang, and V. Grubisic,
813 2008: Mountain waves entering the stratosphere. *J. Atmos. Sci.*, 65, 2543 –2562.

814 [Sun, Y. Q., and F. Zhang, 2015: ~~Intrinsic versus practical limits of atmospheric predictability and~~
815 ~~the significance of the butterfly effect. J. Atmos. Sci., in review.~~](#)

816 Tan, Z. M., F. Zhang, R. Rotunno, and C. Snyder, 2004: Mesoscale predictability of moist
817 baroclinic waves: Experiments with parameterized convection. *J. Atmos. Sci.*, 61, 1794-
818 1804.

819 Torrence, C., and G. P. Compo, 1998: A practical guide to wavelet analysis. *Bull. Amer. Meteor.*
820 *Soc.*, 19, 61 –78.

Fuqing Zhang 5/27/2015 10:13 AM
Deleted: Error growth dynamics within idealized baroclinic waves: i

Fuqing Zhang 5/27/2015 10:14 AM
Deleted: and

Fuqing Zhang 5/27/2015 10:14 AM
Deleted: mesoscale

Fuqing Zhang 5/27/2015 10:14 AM
Deleted: In Manuscript

826 Uccellini, L. W. and S. E. Koch, 1987: The synoptic setting and possible source mechanisms for
827 mesoscale gravity wave events. *Mon. Wea. Rev.*, 115, 721–729.

828 Vaughan G, Worthington RM, 2000: Break-up of a stratospheric streamer observed by MST
829 radar. *Quarterly Journal of the Royal Meteorological Society*, 126, 1751-1769.

830 Vaughan, G., and R. Worthington, 2007: Inertia-gravity waves observed by the UK MST radar,
831 *Q. J. R. Meteorol. Soc.*, 133(S2), 179–188.

832 Vergeiner, I., and D. K. Lilly, 1970: The dynamic structure of lee wave flow as obtained from
833 balloon and airplane observations. *Mon. Wea. Rev.*, 98, 220-232.

834 Vincent, R. A., and M. J. Alexander, 2000: Gravity waves in the tropical lower stratosphere: An
835 observational study of seasonal and interannual variability. *J. Geophys. Res.*, 105, 17, 971-
836 17, 982.

837 Waite, M. L., and Chris Snyder, 2013: Mesoscale Energy Spectra of Moist Baroclinic Waves. *J.*
838 *Atmos. Sci.*, 70, 1242–1256.

839 Wang, L. and M. J. Alexander, T. P. Bui, and M. J. Mahoney, 2006: Small-scale gravity waves
840 in ER-2 MMS/MTP wind and temperature measurements during CRYSTAL-FACE. *Atmos.*
841 *Chem. Phys.*, 6, 1091-1104.

842 Wang, L., and M. A. Geller, 2003: Morphology of gravity-wave energy as observed from 4 years
843 (1998-2001) of high vertical resolution U.S. radiosonde data, *J. Geophys. Res.*, 108 (D16),
844 4489, doi:10.1029/2002JD002786.

845 Wang, S. and F. Zhang, 2007: Sensitivity of mesoscale gravity waves to the baroclinicity of jet-
846 front systems. *Mon. Wea. Rev.*, 135, 670-688.

847 Wei, J., and F. Zhang, 2014: Mesoscale gravity waves in moist baroclinic jet–front systems. *J.*
848 *Atmos. Sci.*, 71, 929–952. doi: <http://dx.doi.org/10.1175/JAS-D-13-0171.1>

849 Wei, J., and F. Zhang, 2015: Tracking gravity waves in moist baroclinic jet-front systems.
850 *Journal of Advanced Modeling in Earth Sciences (JAMES)*, DOI: 10.1002/2014MS000395

851 Woods, B. K. and R. B. Smith, 2010: Energy flux and wavelet diagnostics of secondary
852 mountain waves. *J. Atmos. Sci.*, 67, 3721-3738.

853 Woods, B. K. and R. B. Smith, 2011: Short-Wave Signatures of Stratospheric Mountain Wave
854 Breaking. *J. Atmos. Sci.*, 68, 635-656.

855 Wu, D. L., and F. Zhang, 2004: A study of mesoscale gravity waves over North Atlantic with
856 satellite observations and a mesoscale model. *J. Geophys. Res.-Atmos.*, 109, D22104.

857 Yamanaka, M. D., S. Ogino, S. Kondo, T. Shimomai, S. Fukao, Y. Shibagaki, Y. Maekawa, and
858 I. Takayabu, 1996: Inertio-gravity waves and subtropical multiple tropopauses: vertical
859 wavenumber spectra of wind and temperature observed by the MU radar, radiosondes and
860 operational rawinsonde network. *J. Atmos. Terr. Phys.*, 58, 785-805.

861 Zhang, F., 2004: Generation of mesoscale gravity waves in the upper-tropospheric jet-front
862 systems. *J. Atmos. Sci.*, 61, 440-457.

863 Zhang, F., and S. E. Koch, 2000: Numerical simulation of a gravity wave event over CCOPE.
864 Part II: Wave generated by an orographic density current. *Mon. Wea. Rev.*, 128, 2777– 2796.

865 Zhang, F., M. Zhang, J. Wei, and S. Wang, 2013: Month-Long Simulations of Gravity Waves
866 over North America and North Atlantic in Comparison with Satellite Observations. *Acta*
867 *Meteorologica Sinica*, 27, 446-454.

868 Zhang, F., N. Bei, R. Rotunno, C. Snyder, and C. C. Epifanio, 2007: Mesoscale predictability of
869 moist baroclinic waves: Convection-permitting experiments and multistage error growth
870 dynamics. *J. Atmos. Sci.*, 64, 3579-3594.

871 Zhang, F., S. E. Koch, and M. L. Kaplan, 2003: Numerical simulations of a large-amplitude
872 gravity wave event. *Meteorology and Atmospheric Physics*, 84, 199–216.

873 Zhang, F., S. E. Koch, C. A. Davis, and M. L. Kaplan, 2001: Wavelet analysis and the governing
874 dynamics of a large-amplitude gravity wave event along the east coast of the United States.
875 *Q. J. R. Meteorol. Soc.*, 127, 2209-2245.

876 Zhang, F., S. Wang, and R. Plougonven, 2004: Uncertainties in using the hodograph method to
877 retrieve gravity wave characteristics from individual soundings. *Geophysical Research*
878 *Letters*, 31, L11110, doi:10.1029/2004GL019841.

879 Zhang, F., Z. Meng, and A. Aksoy, 2006: Tests of an ensemble Kalman filter for mesoscale and
880 regional-scale data assimilation. Part I: Perfect model experiments. *Mon. Wea. Rev.*, 134,
881 722-736.

882 Zhang, S. D., and F. Yi, 2007: Latitudinal and seasonal variations of inertial gravity wave
883 activity in the lower atmosphere over central China, *J. Geophys. Res.*, 112, D05109,
884 doi:10.1029/2006JD007487.
885
886

887 **Figure Captions**

888 **Figure 1.** The 68 Gulfstream V (GV) flight segments (colored lines) selected for wave analysis
889 during START08. The 18 colors represent 18 research flight (RF) missions. The thick blue lines
890 represent the second flight (RF02). The grey shadings give the terrain elevation map (shaded
891 every 250 m) over north America. The 4 black boxes are the model domain design for the second
892 research flight (RF02) during 21-22 April 2008, which are named D1-D4 from coarse to fine
893 domain with horizontal resolution as 45 km, 15 km, 5 km and 1.67 km, respectively. The field
894 catalog of the 18 RFs are available online (at
895 http://catalog.eol.ucar.edu/start_08/missions/missions.html). The GV ground tracks of the
896 18 RFs are also documented in Fig. 2 of Pan et al. (2010).

897

898 **Figure 2.** Simulated pressure at 9 km altitude (black contours; unit in hPa ; $\Delta=2hPa$),
899 horizontal wind speed at 9 km altitude (black shadings; unit in ms^{-1} ; levels at 30, 40, 50, 60
900 ms^{-1}), and the mesoscale component of horizontal divergence at 12.5 km (blue contours,
901 positive; red contour, negative; contour levels at $\pm 7.5, \pm 15, \pm 30, \pm 60 \times 10^{-5} s^{-1}$) during RF02
902 in START08, with marked GV flight track (blue line) at selected time: (a) entire flight track at 21
903 April 18:00 UTC, (b) segment J1 at 21 April 19:10 UTC, (c) segment J2 at 21 April 19:50 UTC,
904 (d) segment J3 at 21 April 22:10 UTC, (e) segment M1 at 21 April 23:10 UTC, and (f) segment
905 M2 at 22 April 00:20 UTC. The triangle and circle marks represent the aircraft at the start time
906 of the segment and at selected time. The two-dimensional (2D) variables are based on D4 in Fig.
907 1. A band-pass filter is applied to extract signals with wavelength from 50 to 500 km for
908 horizontal divergence.

909

910 **Figure 3.** GV flight-level aircraft measurements during 5 selected segments (from left to right:
911 J1, J2, J3, M1 and M2) of RF02 in START08: (a) along-track velocity component (red; unit in
912 ms^{-1} ; left y axis), across-track velocity component (blue; unit in ms^{-1} ; right y axis) and
913 horizontal velocity component (black; unit in ms^{-1} ; left y axis), (b) vertical velocity component
914 (red; unit in ms^{-1} ; left y axis) and potential temperature (blue; unit in K ; right y axis), (c)
915 perturbation of hydrostatic pressure correction (red; unit in hPa ; left y axis), static pressure
916 (blue; unit in hPa ; right y axis) and corrected static pressure (black; unit in hPa ; left y axis), and
917 (d) flight height (red; unit in km ; left y axis) and terrain (blue; black shading below terrain; unit
918 in km ; right y axis). The series in segment J3 and M2 are reversed to facilitate the comparison
919 with J1+J2 and M1, respectively. Therefore, the orientation of x axis is from west to east along
920 each flight segment. The distance between minor tick marks in x axis is 100 km. The
921 perturbations in (c) are defined as the differences between the original data and their mean from
922 their corresponding segments.

923

924 **Figure 4.** The spectrum (black line) of GV flight-level aircraft measurement during 5 selected
925 segments (from left to right: J1, J2, J3, M1 and M2) of RF02 in START08: (a) along-track
926 velocity component (unit: $m^2s^{-2} \cdot m$), (b) across-track velocity component (unit: $m^2s^{-2} \cdot m$), (c)
927 vertical velocity component (unit: $m^2s^{-2} \cdot m$), (d) potential temperature (unit: $K^2 \cdot m$), and (e)
928 corrected static pressure (unit: $hPa^2 \cdot m$). Green lines show the theoretical Markov spectrum and
929 the 5% and 95% confidence curves using the lag 1 autocorrelation. The blue (red) reference lines
930 have slopes of $-5/3$ (-3).

931

932 **Figure 5.** Composite spectrum (black line) of GV flight-level aircraft measurement averaging
933 over all 68 segments in START08 (colored lines in Fig. 1): (a) along-track velocity component
934 (unit: $m^2s^{-2} \cdot m$), (b) across-track velocity component (unit: $m^2s^{-2} \cdot m$), (c) vertical velocity
935 component (unit: $m^2s^{-2} \cdot m$), (d) horizontal velocity component (unit: $m^2s^{-2} \cdot m$), (f) potential
936 temperature (unit: $K^2 \cdot m$), (g) corrected static pressure (unit: $hPa^2 \cdot m$), (h) static pressure
937 (unit: $hPa^2 \cdot m$), and (i) hydrostatic pressure correction (unit: $hPa^2 \cdot m$). The subplot (e) kinetic
938 energy (unit: $m^2s^{-2} \cdot m$) is the sum of (a)-(c). Green lines show the composite curves of the
939 theoretical Markov spectrum and the 5% and 95% confidence curves using the lag 1
940 autocorrelation. The blue (red) reference lines have slopes of -5/3 (-3).

941

942 **Figure 6.** Wavelet power spectrum of GV flight-level aircraft measurement during 5 selected
943 segments (from left to right: J1, J2, J3, M1 and M2) of RF02 in START08: (a) along-track
944 velocity component, (b) across-track velocity component, (c) vertical velocity component, (d)
945 potential temperature, and (e) corrected static pressure. Reference line (black line) shows the
946 cone of influence (COI), and the area outside COI is where edge error becomes important. Black
947 contour lines with dot shading represent 95% significance level based on a red noise background
948 (also see Torrence and Compo 1998; Woods and Smith 2010). The x axis is the same as in Fig.
949 3, including the reversal of segment J3 and M2.

950

951 **Figure 7.** The wavelet cospectrum of (a) $(u'w')_c$, (b) $(v'w')_c$, (c) $(p'_c w')_c$, (d) the quadrature
952 spectrum of $(\theta'w')_q$, and (e) the absolute coherence phase angle of $(\theta'w')_p$ for GV flight-level
953 aircraft measurement during 5 selected segments (from left to right: J1, J2, J3, M1 and M2) of
954 RF02 in START08. Reference line (black line) shows the cone of influence (COI), and the area

955 outside COI is where edge error becomes important. Black contour lines with dot shading
956 represent 95% significance level (also see Torrence and Compo 1998; Woods and Smith 2010).
957 The x axis is the same as in Fig. 3, including the reversal of segment J3 and M2. The horizontal
958 black line marks the scale of 50 km.

959

960 **Figure 8.** A relatively good/clean example of mesoscale variations during segment J3 (location
961 250-360 km): (a) along-track velocity component (red; unit in m/s) and vertical velocity
962 component (blue; unit in m/s), (b) across-track velocity component (red; unit in m/s) and vertical
963 velocity component (blue; unit in m/s), (c) along-track velocity component (red; unit in m/s) and
964 across-track velocity component (blue; unit in m/s), (d) corrected static pressure (red; unit in
965 hPa) and along-track velocity component (blue; unit in m/s), (e) corrected static pressure (red;
966 unit in hPa) and across-track velocity component (blue; unit in m/s), (f) corrected static pressure
967 (red; unit in hPa) and vertical velocity component (blue; unit in m/s), (g) potential temperature
968 (red; unit in K) and vertical velocity component (blue; unit in m/s), (h) static pressure (red; unit
969 in hPa) and vertical velocity component (blue; unit in m/s), and (i) hydrostatic pressure
970 correction (red; unit in hPa) and vertical velocity component (blue; unit in m/s). A wavelet-based
971 band-pass filter is applied to extract signals with wavelength from 100 to 120 km for all the
972 above flight variables.

973

974 **Figure 9.** Same as in Fig. 8, but for a relatively bad/noisy example of mesoscale variations
975 during segment J3 (location 560-688 km). The wavelet-based band-pass window is 118-138 km.

976

977 **Figure 10.** Same as in Fig. 8, but for a relatively good/clean example of smaller-scale variations
978 during segment J3 (location 650-750 km). The wavelet-based band-pass window is 32-64 km.

979

980 **Figure 11.** Same as in Fig. 8, but for an example of smaller-scale variations during segment J3
981 (location 680-780 km). The wavelet-based band-pass window is 8-16 km.

982

983 **Figure 12.** (a) The spectrum of corrected static pressure (black), static pressure (blue), and
984 hydrostatic pressure correction (red) based on GV flight-level aircraft measurement during 5
985 selected segments (from left to right: J1, J2, J3, M1 and M2) of RF02 in START08. (b) The
986 spectrum of the square root ratio (see the text for its definition).

987

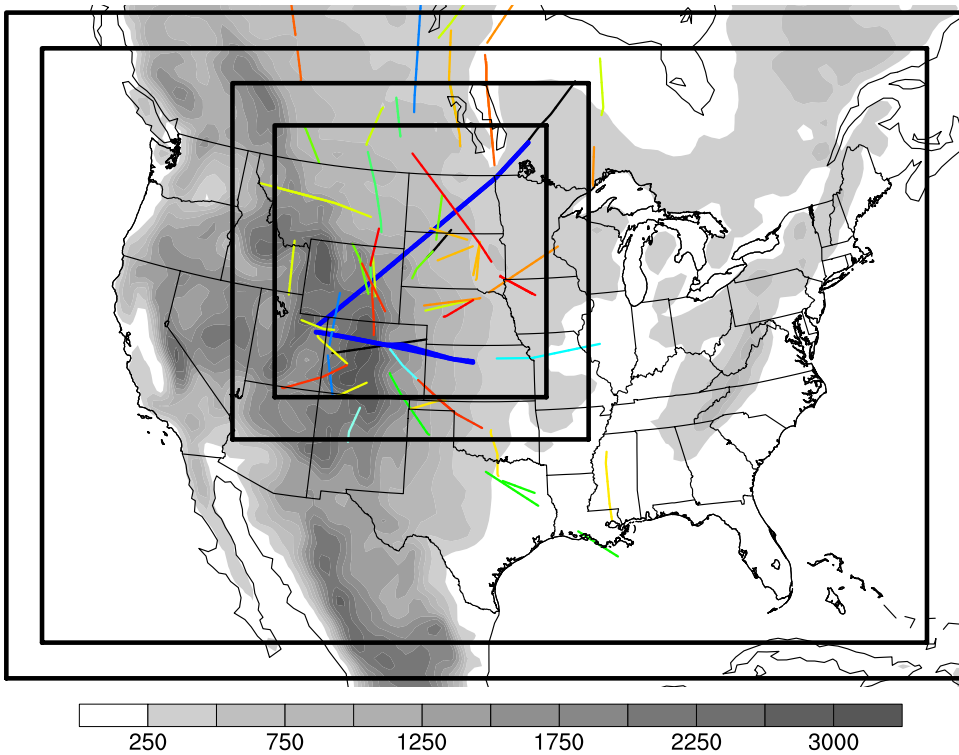
988

989 **Table 1:** The aircraft statistic parameters of five selected flight segment in RF02 during the
990 START08 field campaign. Column 1-7 represent the name, the starting time (s), the ending time
991 (s), the averaged flight height (km), the averaged static pressure (hPa), the total distance (km),
992 and the averaged flight speed (m/s) of each selected flight segment.
993

Flight Segment	Start (s)	End (s)	Averaged Flight Height (km)	Averaged Static Pressure (hPa)	Distance (km)	Averaged Flight Speed (m/s)
J1	2450	5000	11.8	196.9	685.74	268.92
J2	5170	8620	12.5	178.7	908.53	263.34
J3	9120	16850	13.1	162.1	1641.93	212.41
M1	17100	20630	12.6	178.5	950.46	269.25
M2	21500	26430	11.0	227.6	946.90	192.07

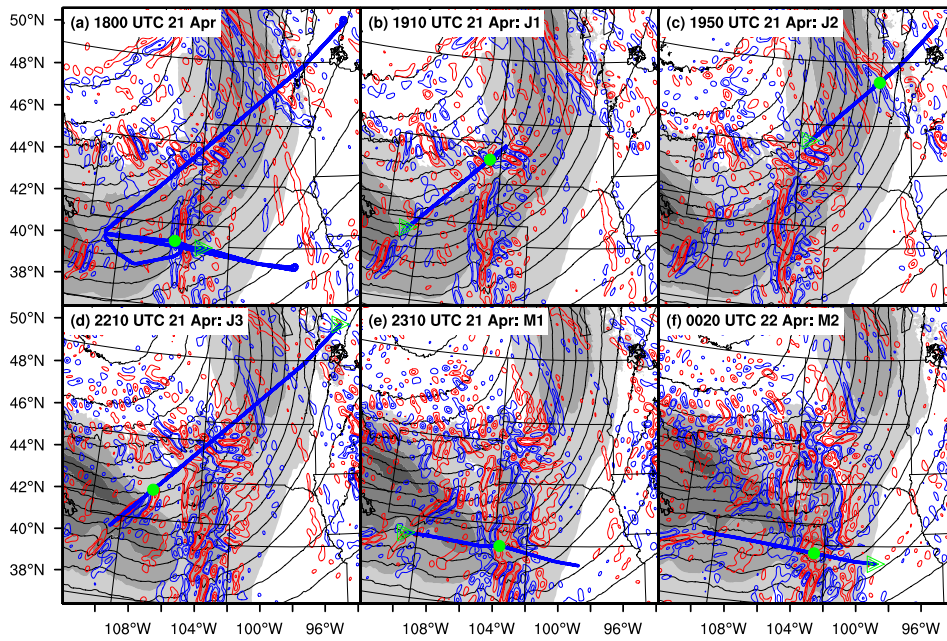
994

995

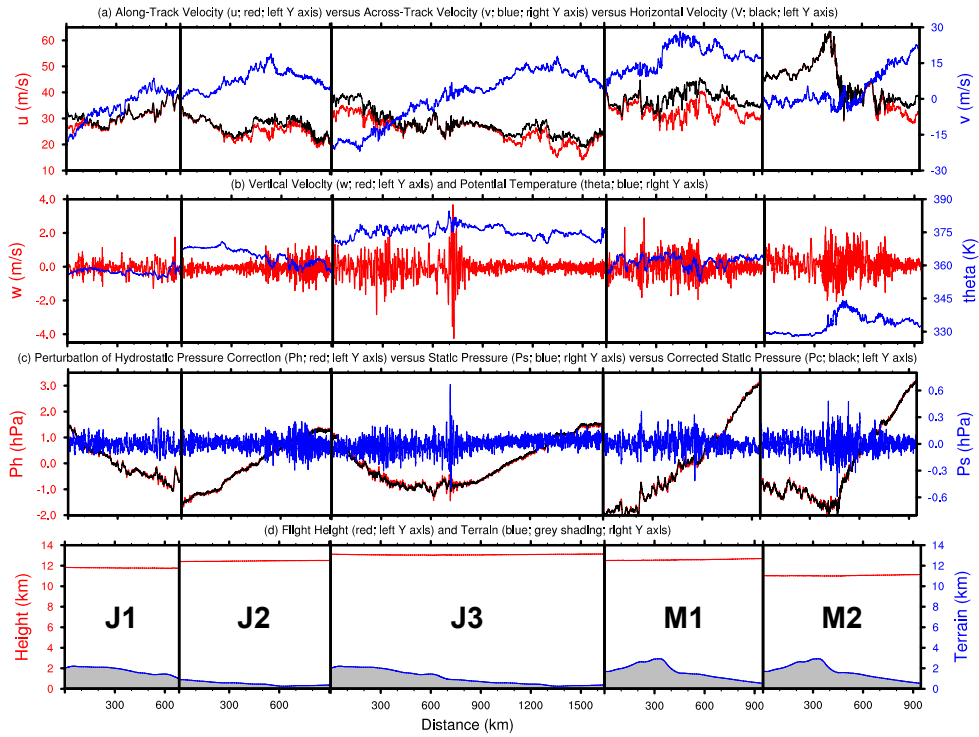


996

997 **Figure 1.** The 68 Gulfstream V (GV) flight segments (colored lines) selected for wave analysis
 998 during START08. The 18 colors represent 18 research flight (RF) missions. The thick blue lines
 999 represent the second flight (RF02). The grey shadings give the terrain elevation map (shaded
 1000 every 250 m) over north America. The 4 black boxes are the model domain design for the second
 1001 research flight (RF02) during 21-22 April 2008, which are named D1-D4 from coarse to fine
 1002 domain with horizontal resolution as 45 km, 15 km, 5 km and 1.67 km, respectively. The field
 1003 catalog of the 18 RFs are available online (at
 1004 http://catalog.eol.ucar.edu/start_08/missions/missions.html). The GV ground tracks of the 18
 1005 RFs are also documented in Fig. 2 of Pan et al. (2010).
 1006

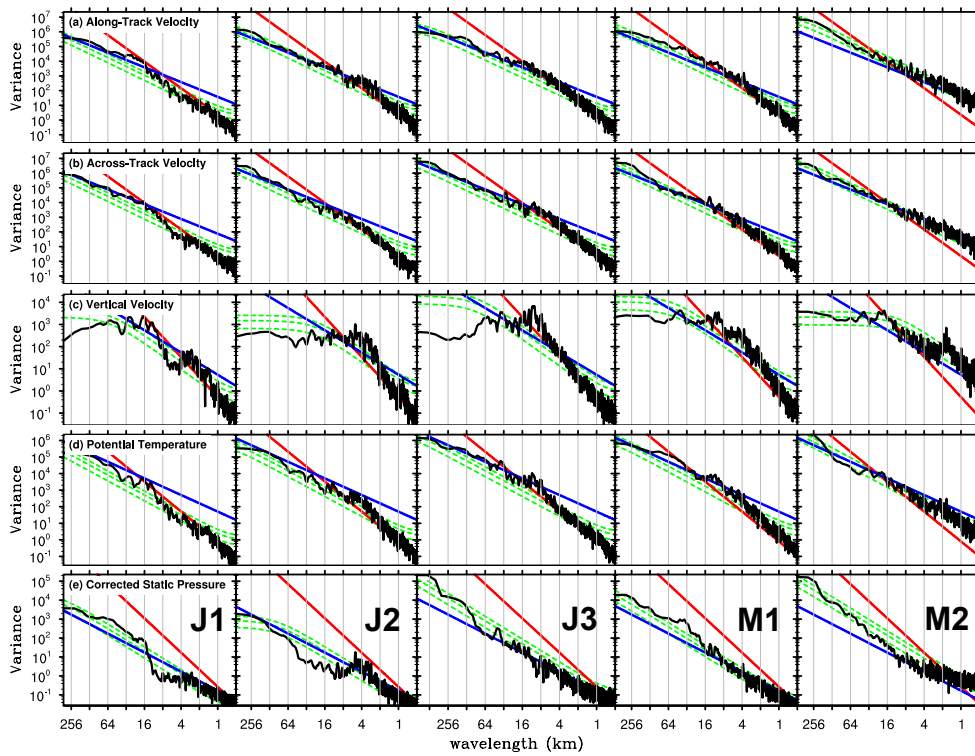


1007
 1008 **Figure 2.** Simulated pressure at 9 km altitude (black contours; unit in hPa ; $\Delta=2hPa$),
 1009 horizontal wind speed at 9 km altitude (black shadings; unit in ms^{-1} ; levels at 30, 40, 50, 60
 1010 ms^{-1}), and the mesoscale component of horizontal divergence at 12.5 km (blue contours,
 1011 positive; red contour, negative; contour levels at $\pm 7.5, \pm 15, \pm 30, \pm 60 \times 10^{-5} s^{-1}$) during RF02
 1012 in START08, with marked GV flight track (blue line) at selected time: (a) entire flight track at 21
 1013 April 18:00 UTC, (b) segment J1 at 21 April 19:10 UTC, (c) segment J2 at 21 April 19:50 UTC,
 1014 (d) segment J3 at 21 April 22:10 UTC, (e) segment M1 at 21 April 23:10 UTC, and (f) segment
 1015 M2 at 22 April 00:20 UTC. The triangle and circle marks represent the aircraft at the start time
 1016 of the segment and at selected time. The two-dimensional (2D) variables are based on D4 in Fig.
 1017 1. A band-pass filter is applied to extract signals with wavelength from 50 to 500 km for
 1018 horizontal divergence.
 1019



1020

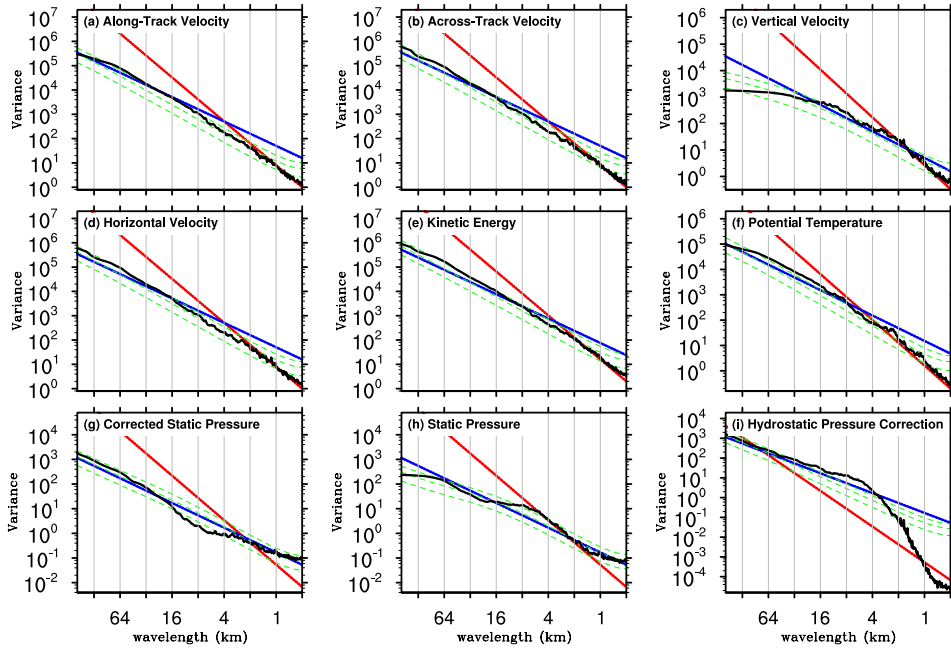
1021 **Figure 3.** GV flight-level aircraft measurements during 5 selected segments (from left to right:
 1022 J1, J2, J3, M1 and M2) of RF02 in START08: (a) along-track velocity component (red; unit in
 1023 ms^{-1} ; left y axis), across-track velocity component (blue; unit in ms^{-1} ; right y axis) and
 1024 horizontal velocity component (black; unit in ms^{-1} ; left y axis), (b) vertical velocity component
 1025 (red; unit in ms^{-1} ; left y axis) and potential temperature (blue; unit in K ; right y axis), (c)
 1026 perturbation of hydrostatic pressure correction (red; unit in hPa ; left y axis), static pressure
 1027 (blue; unit in hPa ; right y axis) and corrected static pressure (black; unit in hPa ; left y axis), and
 1028 (d) flight height (red; unit in km ; left y axis) and terrain (blue; black shading below terrain; unit
 1029 in km ; right y axis). The series in segment J3 and M2 are reversed to facilitate the comparison
 1030 with J1+J2 and M1, respectively. Therefore, the orientation of x axis is from west to east along
 1031 each flight segment. The distance between minor tick marks in x axis is 100 km. The
 1032 perturbations in (c) are defined as the differences between the original data and their mean from
 1033 their corresponding segments.



1034

1035 **Figure 4.** The spectrum (black line) of GV flight-level aircraft measurement during 5 selected
 1036 segments (from left to right: J1, J2, J3, M1 and M2) of RF02 in START08: (a) along-track
 1037 velocity component (unit: $m^2s^{-2} \cdot m$), (b) across-track velocity component (unit: $m^2s^{-2} \cdot m$), (c)
 1038 vertical velocity component (unit: $m^2s^{-2} \cdot m$), (d) potential temperature (unit: $K^2 \cdot m$), and (e)
 1039 corrected static pressure (unit: $hPa^2 \cdot m$). Green lines show the theoretical Markov spectrum and
 1040 the 5% and 95% confidence curves using the lag 1 autocorrelation. The blue (red) reference lines
 1041 have slopes of $-5/3$ (-3).

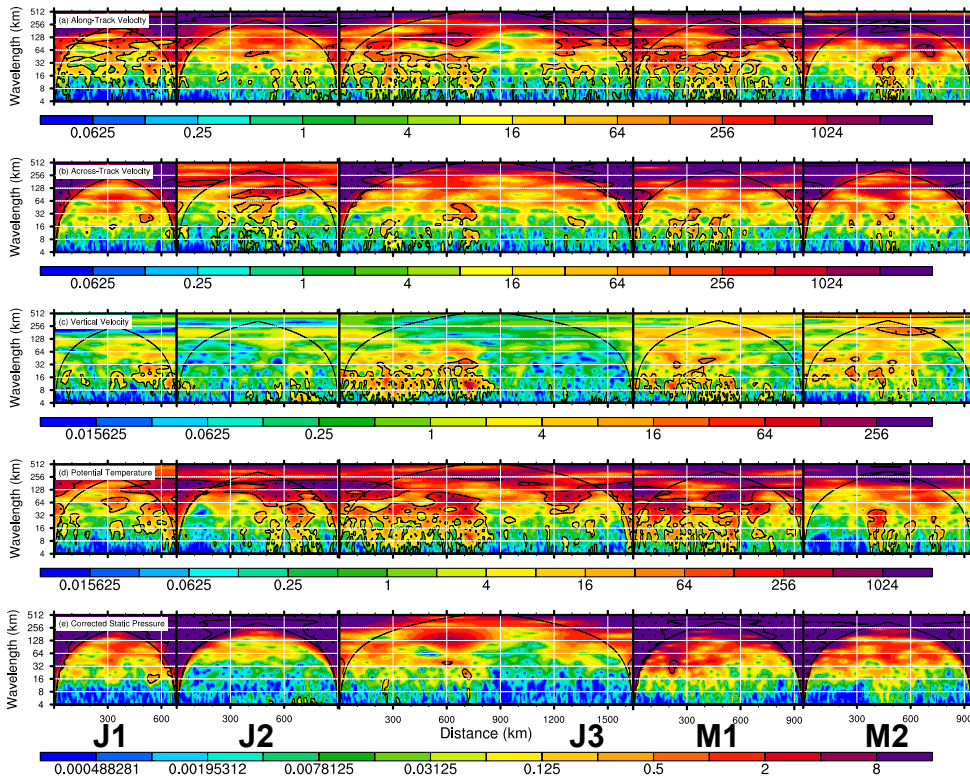
1042



1043

1044 **Figure 5.** Composite spectrum (black line) of GV flight-level aircraft measurement averaging
 1045 over all 68 segments in START08 (colored lines in Fig. 1): (a) along-track velocity component
 1046 (unit: $m^2s^{-2} \cdot m$), (b) across-track velocity component (unit: $m^2s^{-2} \cdot m$), (c) vertical velocity
 1047 component (unit: $m^2s^{-2} \cdot m$), (d) horizontal velocity component (unit: $m^2s^{-2} \cdot m$), (f) potential
 1048 temperature (unit: $K^2 \cdot m$), (g) corrected static pressure (unit: $hPa^2 \cdot m$), (h) static pressure
 1049 (unit: $hPa^2 \cdot m$), and (i) hydrostatic pressure correction (unit: $hPa^2 \cdot m$). The subplot (e) kinetic
 1050 energy (unit: $m^2s^{-2} \cdot m$) is the sum of (a)-(c). Green lines show the composite curves of the
 1051 theoretical Markov spectrum and the 5% and 95% confidence curves using the lag 1
 1052 autocorrelation. The blue (red) reference lines have slopes of $-5/3$ (-3).

1053



1054

1055

1056

1057

1058

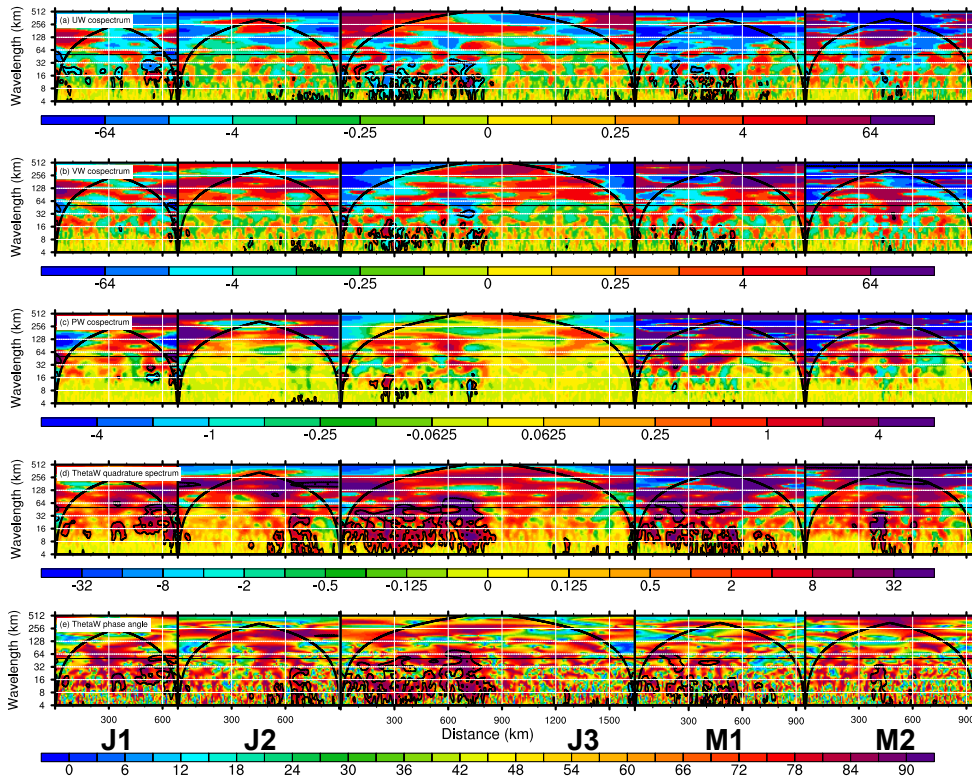
1059

1060

1061

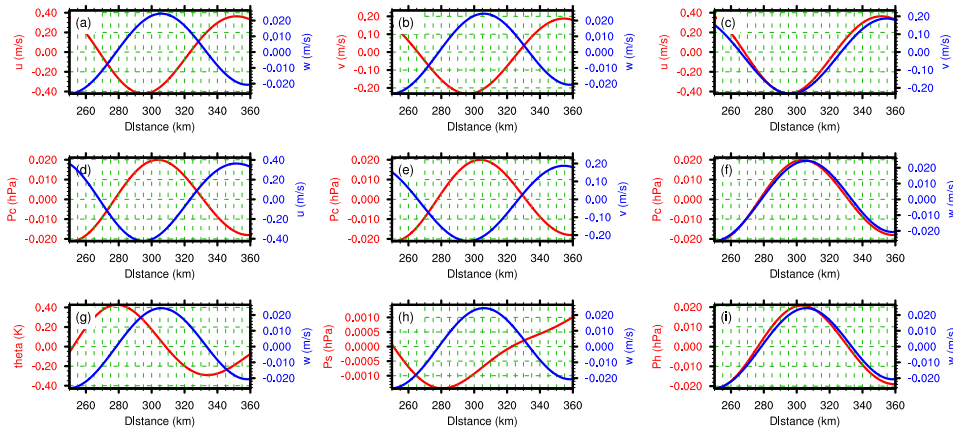
1062

Figure 6. Wavelet power spectrum of GV flight-level aircraft measurement during 5 selected segments (from left to right: J1, J2, J3, M1 and M2) of RF02 in START08: (a) along-track velocity component, (b) across-track velocity component, (c) vertical velocity component, (d) potential temperature, and (e) corrected static pressure. Reference line (black line) shows the cone of influence (COI), and the area outside COI is where edge error becomes important. Black contour lines with dot shading represent 95% significance level based on a red noise background. The x axis is the same as in Fig. 3, including the reversal of segment J3 and M2.



1063
 1064 **Figure 7.** The wavelet cospectrum of (a) $(u'w')_c$, (b) $(v'w')_c$, (c) $(p_c'w')_c$, (d) the quadrature
 1065 spectrum of $(\theta'w')_q$, and (e) the absolute coherence phase angle of $(\theta'w')_p$ for GV flight-level
 1066 aircraft measurement during 5 selected segments (from left to right: J1, J2, J3, M1 and M2) of
 1067 RF02 in START08. Reference line (black line) shows the cone of influence (COI), and the area
 1068 outside COI is where edge error becomes important. Black contour lines with dot shading
 1069 represent 95% significance level. The x axis is the same as in Fig. 3, including the reversal of
 1070 segment J3 and M2. The horizontal black line marks the scale of 50 km.
 1071

Segment J3 (distance: 250-360km; bandpass window: 100-120km)



1072

1073

1074

1075

1076

1077

1078

1079

1080

1081

1082

1083

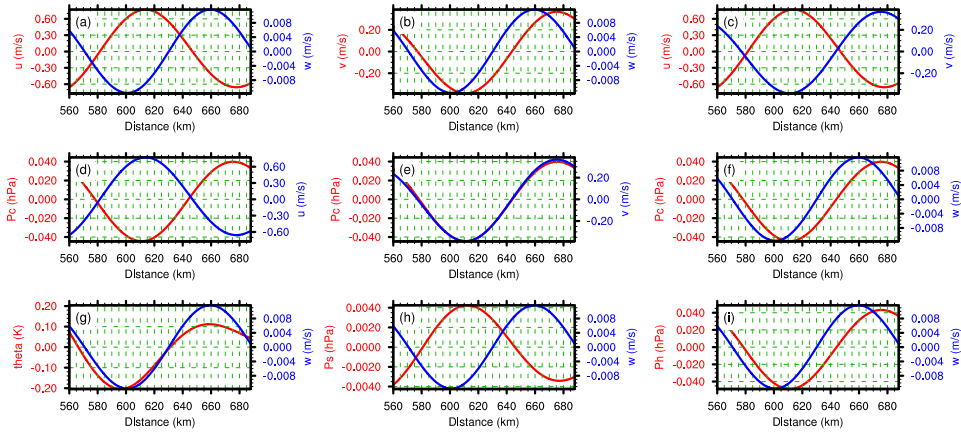
1084

1085

1086

Figure 8. A relatively good/clean example of mesoscale variations during segment J3 (location 250-360 km): (a) along-track velocity component (red; unit in m/s) and vertical velocity component (blue; unit in m/s), (b) across-track velocity component (red; unit in m/s) and vertical velocity component (blue; unit in m/s), (c) along-track velocity component (red; unit in m/s) and across-track velocity component (blue; unit in m/s), (d) corrected static pressure (red; unit in hPa) and along-track velocity component (blue; unit in m/s), (e) corrected static pressure (red; unit in hPa) and across-track velocity component (blue; unit in m/s), (f) corrected static pressure (red; unit in hPa) and vertical velocity component (blue; unit in m/s), (g) potential temperature (red; unit in K) and vertical velocity component (blue; unit in m/s), (h) static pressure (red; unit in hPa) and vertical velocity component (blue; unit in m/s), and (i) hydrostatic pressure correction (red; unit in hPa) and vertical velocity component (blue; unit in m/s). A wavelet-based band-pass filter is applied to extract signals with wavelength from 100 to 120 km for all the above flight variables.

Segment J3 (distance: 560-688km; bandpass window: 118-138km)



1087

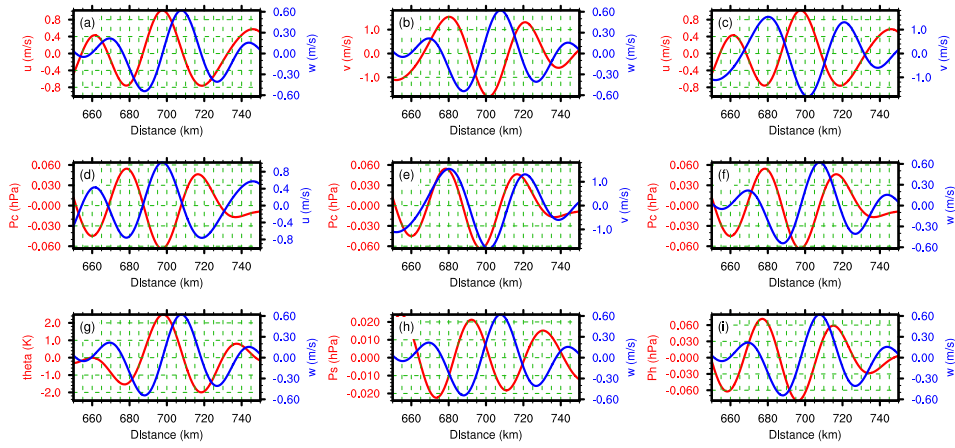
1088

Figure 9. Same as in Fig. 8, but for a relatively bad/noisy example of mesoscale variations during segment J3 (location 560-688 km). The wavelet-based band-pass window is 118-138 km.

1089

1090

Segment J3 (distance: 650-750km; bandpass window: 32-64km)



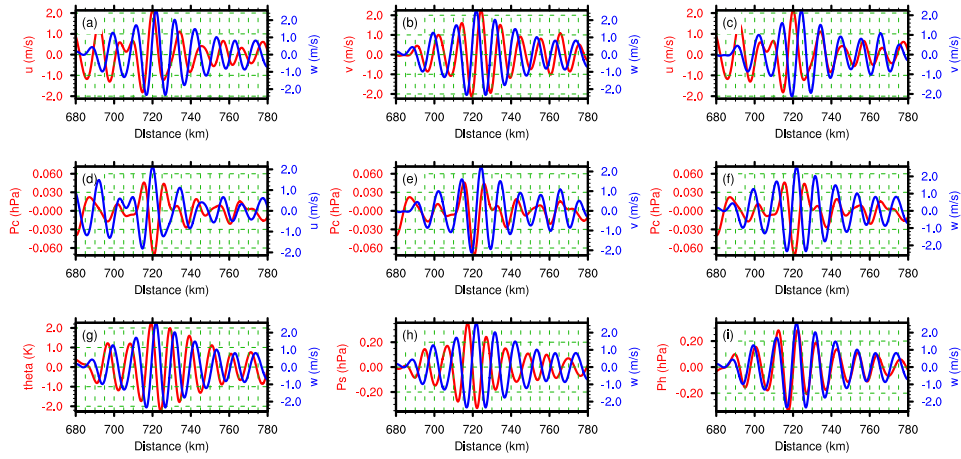
1091

1092 **Figure 10.** Same as in Fig. 8, but for a relatively good/clean example of smaller-scale variations

1093 during segment J3 (location 650-750 km). The wavelet-based band-pass window is 32-64 km.

1094

Segment J3 (distance: 680-780km; bandpass window: 8-16km)

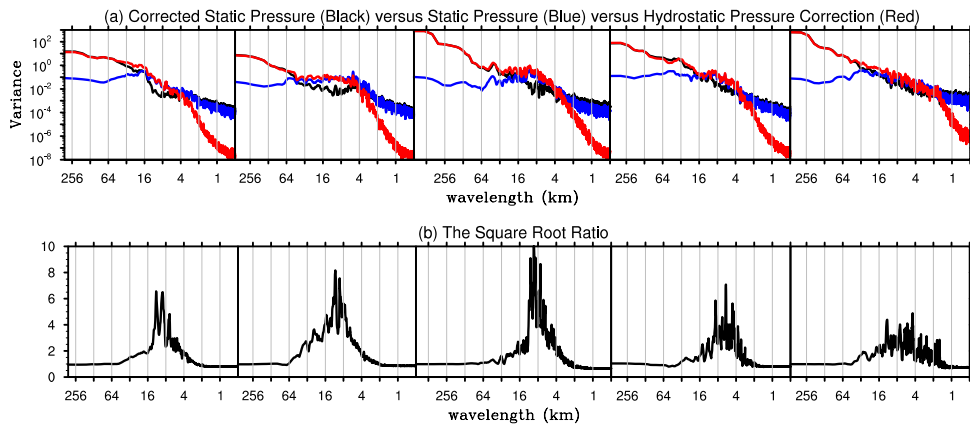


1095

1096 **Figure 11.** Same as in Fig. 8, but for an example of smaller-scale variations during segment J3

1097 (location 680-780 km). The wavelet-based band-pass window is 8-16 km.

1098



J1 J2 J3 M1 M2

1099 **Figure 12.** (a) The spectrum of corrected static pressure (black), static pressure (blue), and
 1100 hydrostatic pressure correction (red) based on GV flight-level aircraft measurement during 5
 1101 selected segments (from left to right: J1, J2, J3, M1 and M2) of RF02 in START08. (b) The
 1102 spectrum of the square root ratio (see the text for its definition).
 1103
 1104